Interacting wind- and tide-forced boundary-layers in a large strait

A. F. Valcarcel[1,2], C. L. Stevens[2,3], J. M. O'Callaghan[2], S. H. Suanda[4]

[1]University of Otago, Department of Marine Science, Dunedin, New Zealand
[2]National Institute of Water and Atmospheric research, Ocean Observations, Wellington, New Zealand
[3]University of Auckland, Department of Physics, Auckland, New Zealand
[4]University of North Carolina in Wilmington, Department of Physics and Physical Oceanography, Wilmington, USA

Key Points:

- $\mathcal{O}(40,000)$ estimates of turbulence from glider microstructure sampling and direct flow-through-water spectral conversion show interactions between wind and tidally-forced boundary-layers throughout the water depth
- Enhanced dissipation is associated with sub-marginal (i) dynamical stability (median $Ri_g = 0.14 < 1/4$ in observations) and (ii) mixing efficiency (median $R_f = 0.1 < 0.17$ in 1D turbulence model results)
- Transient stratification reduces diapycnal mixing (by up to two orders of magnitude), stabilizes the mean flow (median $Ri_g = 0.61 > 1/4$) and creates turbulence anisotropy ($\mathcal{O}(100)$ samples with $Re_b < 10^2$)

Corresponding author: A. F. Valcarcel, arnaud.valcarcel@niwa.co.nz

Abstract

Observations of the spatio-temporal structure of turbulent mixing in a large, energetic strait were used to examine the interactions between wind- and tidally-forced boundary layers in a coastal environment. Te Moana-o-Raukawa (Cook Strait) of Aotearoa (New Zealand) is a relatively wide, energetic strait, known to experience substantial tidal currents and wind stress. A turbulence-enabled ocean glider mission measured $\mathcal{O}(40,000)$ turbulence samples that passed QAQC including the use of a vehicle-mounted speed through water sensor. The observations were compared to one-dimensional models of turbulence to understand the mechanisms that regulates the vertical structure of mixing. Tidal flows of $\mathcal{O}(1\,\mathrm{m\,s^{-1}})$ and wind speeds of $\mathcal{O}(10\,\mathrm{m\,s^{-1}})$ enhance dissipation to $\epsilon = \mathcal{O}(10^{-5}\mathrm{W\,kg^{-1}})$ through boundary drag, shear-driven production of turbulent kinetic energy (P) and to a minor extent buoyancy flux (G). The benthic and wind-driven boundary layers behaved reasonably predictably when considering a 1D perspective. The interaction between the two boundary layers depended on mid-water column stratification which is to a large degree an externally-prescribed condition. Transient stratification can stabilize the mean flow (median $Ri_g = 0.6(> 1/4)$) and reduce both turbulence intensity (Re_b) and diapycnal diffusivity (K_z) by up to two orders of magnitude in the middle of the water column, insulating bottom and surface mixing-layers. Mid-water dissipation rate levels tend to be associated with marginal dynamical stability (median $Ri_g = 0.22(\sim 1/4)$) and canonical mixing efficiency (median $R_f = 0.17$), while elevated levels are connected to unstable mean flow conditions (median $Ri_g = 0.14(< 1/4)$) and reduced mixing efficiency (median $R_f = 0.1(< 0.17)$) that promotes turbulence growth.

Plain Language Summary

The coastal oceans are very active regions of the planet because of how tides and meteorology interact in shallow water to create ocean mixing. Consequently there is a lot of biological activity as well as absorption of CO_2. However, these highly energetic waters also means it is hard to measure mixing. In this study we describe results from a robotic underwater glider that drifted through the very turbulent waters of Te Moana-o-Raukawa (Cook Strait) that separates the two main islands of Aotearoa (New Zealand). The glider was configured to measure ocean properties that allow us to estimate how energy is transferred from the winds and tides to processes that aid biological production and CO_2 absorption. We found that boundary-layers formed by wind and tides typically can impact the water from surface to seafloor, except when pockets of fresher or warmer water find their way into the region.

1 Introduction

Turbulent mixing in the coastal ocean regulates stratification, air-sea exchanges and nutrient fluxes for a key region of the Earth system (Sandstrom & Elliott, 1984; Aikman, 1984; Sharples et al., 2001; MacKinnon & Gregg, 2005b), thus having global implications for biological productivity and the uptake of atmospheric CO_2 (Simpson & Sharples, 2012; Muller-Karger et al., 2005; Borges et al., 2005; Bianchi et al., 2005; Thomas et al., 2004; Becherer et al., 2022). Primary drivers for this mixing come from currents and wind - processes that operate independently but interact. Enhanced mixing in the bottom boundary layer has shown to impact the transport of sediments that shape seafloor topography (Cacchione et al., 2002; Zulberti et al., 2020) and to facilitate the supply of nutrient-rich waters to the pycnocline to support primary production (Becherer et al., 2022). Wind stress in the surface boundary layer can promote gas exchanges and heat uptake (Thomas et al., 2004), enrich the euphotic zone with nutrients (Chiswell et al., 2017) and accelerate the destruction of stratification in shallow shelf seas thermocline especially during storms (Schultze et al., 2020).

The study of turbulent mixing in the ocean lies in the intersections between observations and energetics budgets (Polzin & McDougall, 2022). For Turbulent Kinetic Energy (TKE, notation k), the balance equation can be represented by Reynolds decomposition in idealized Boussinesq-fluid formulation (Polzin & McDougall, 2022; Umlauf et al., 2012) as:

$$\dot{k} = T_k + P + G - \epsilon \quad [\mathrm{W\,kg^{-1}}], \tag{1}$$

where $\dot{k}$ is the material derivative (includes temporal derivative and advection terms) of TKE. P, G and ϵ are the rates of shear production, buoyancy production/destruction and dissipation of TKE, respectively. T_k represents the viscous and turbulent transport. To quantify buoyancy fluxes across isopycnals Osborn (1980) assumed a statistically steady balance between total production and dissipation of TKE ($P+G \sim \epsilon$) and ignored transport terms (Gregg et al., 2017; Caulfield, 2020) to formulate the vertical diffusivity of mass:

$$K_z = \frac{R_f}{1 - R_f} \frac{\epsilon}{N^2} \; [\mathrm{m^2\,s^{-1}}], \tag{2}$$

where $R_f = -G/P$ is the flux Richardson number, often referred to as the mixing efficiency: the proportion of change in background potential energy from an expended amount of energy, generally assumed as a constant of $R_f = 0.17$ ($R_f/(1 - R_f) = 0.2$) (see Gregg et al. (2017) for a review). Here, $\epsilon = \nu/2.\overline{(\partial_j u_i + \partial_i u_j)^2}$ [$\mathrm{W\,kg^{-1}}$] and $N^2 = -g/\rho_0.\partial_z \rho$ [$\mathrm{s^{-2}}$], with ν the kinematic viscosity of seawater, $\partial_j u_i$ and $\partial_i u_j$ the velocity shear components, g the gravitation constant and ρ (ρ_0) is density (at a reference depth), are two readily observable quantities in the ocean using measurements of microstructure shear (R. Lueck, 2002; Wolk et al., 2009) and temperature-conductivity-depth. From those measures one can estimate the buoyancy Reynolds number

$$Re_b = \frac{\epsilon}{\nu N^2} \; [-], \tag{3}$$

which quantifies the intensity (or level of activity (Schultze et al., 2017)) of turbulence-driven mixing, where high values $Re_b > 1 \times 10^2$ indicate fully developed and isotropic turbulence (Schultze et al., 2017; Bouffard & Boegman, 2013; Shih et al., 2005). Additionally, the dynamical stability of the water column (Ri_g, the gradient Richardson number) as represented by the balance of large scale velocity shear $S^2 = (\partial_z U)^2 + (\partial_z V)^2$ [s^{-2}] (U and V are the mean flow horizontal velocity components) against the stabilizing stratification:

$$Ri_g = \frac{N^2}{S^2} \; [-], \tag{4}$$

which can indicate weak stratification ($Ri_g < 1$) and shear instability ($Ri_g < 1/4$) has also shown to influence mixing efficiency (Salehipour et al., 2016; Caulfield, 2020) and the state of criticality of stratified turbulence (Smyth et al., 2019), indicating that this quantity should be routinely reported on with field measurements when possible (Gregg et al., 2017).

Analysis of turbulent mixing, a patchy and intermittent process in the ocean (Waterhouse et al., 2014), and the interplay of turbulent mixing-layers under strong wind and tidal stress have been recently facilitated by ocean gliders. Gliders are autonomous underwater vehicles that use internal buoyancy adjustements to dive and climb in the ocean interior (Jones et al., 2005) and can be set up to sample near-surface waters even in strong winds (Fer et al., 2014; Peterson & Fer, 2014; Schultze et al., 2020). Measurements of mean flow properties and turbulence-driven mixing from mounted sensors on gliders have led to significant advances in understanding turbulence in the near-surface (St. Laurent & Merrifield, 2017; Lucas et al., 2019), shelf seas (Schultze et al., 2017, 2020) and deep ocean (Naveira Garabato et al., 2019). These extensive datasets can be combined with results from one-dimensional turbulence models as GOTM (General Ocean Turbulence Model, Umlauf and Burchard (2005)), to quantify the vertical transport of TKE (Eq. 1) and the rates at which turbulence is produced or destroyed, and thus analyse shelf seas

stratification and mixing variability from wind and tides forcing (Rippeth et al., 2001; Simpson et al., 2002; Rippeth et al., 2009; Becherer et al., 2022).

Here we present observations and model results of turbulent mixing in a coastal ocean system, Te Moana O Raukawa - Cook Strait, the oceanic passage that separates the two main islands of Aotearoa - New Zealand. Cook Strait is a relatively wide strait, topographically complex, a portion of Greater Cook Strait, a region of considerable submesoscale variability (Stevens, 2014; Jhugroo et al., 2020). Stevens (2018) sampled turbulent mixing in the region using a loose-tethered Vertical Microstructure Profiler (VMP, Rockland Scientific Instruments) and showed high levels of dissipation rates (linear average of $\epsilon = 2 \times 10^{-6}\,\mathrm{W\,kg^{-1}}$) in a low stratification ($1 \times 10^{-7} < N^2 < 1 \times 10^{-4}\,\mathrm{s^{-1}}$) environment. This amounted to intense turbulence (peak of the Re_b distribution around $5{\times}10^4$) and high values of diapycnal diffusivity (K_z peaking close to $1\,\mathrm{m^2\,s^{-1}}$) (Osborn, 1980). Surprisingly, however intense the mixing and homogenization of the water column, persistent stratification has been observed in the strait (Stevens, 2014).

This paper uses microstructure data from an ocean glider, background flow velocities from an Acoustic Doppler Profiler (ADCP), wind records from weather stations and one-dimensional model results to address the impacts of geophysical forcings on the spatio temporal variability of turbulent mixing in a tidal channel, Cook Strait. After introducing the datasets and methodology (Section 2), presenting observations and models (Section 3), we discuss how our results address the following questions: (Section 4.1) How do the surface and bottom mixing-layers compare with one-dimensional paradigms? (Section 4.2) Does weak stratification in the strait act as a vertical barrier to mixing? (Section 4.3) Do dynamical instability and critical mixing efficiency drive elevated dissipation rates? (Section 4.4) How does the mixing observed in Cook Strait compare with observations from broadly similar systems? Finally we draw conclusions for this study and outline future work (Section 5).

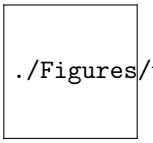

Figure 1. Maps of (a) Aotearoa - New Zealand; Location of (b) the ADCP (blue square marker), the Cape Campbell atmospheric sampling station (orange triangle marker), the glider surfacing locations (colored circular markers) and the topography of Te Moana o Raukawa - Cook Strait (colorbar); (c) a zoomed-in window showing the current profiler and the glider surfacing tracks coloured per time of the sampling window.

2 Methods

2.1 Location

Cook Strait Narrows is an ideal location to study interacting boundary layers as it experiences very fast tidally driven flows (e.g. flows as fast as $3.4\,\mathrm{m\,s^{-1}}$ during spring tides (Stevens et al., 2012)) and high winds (Vennell & Collins, 1991; Zeldis et al., 2013). The Narrows are on average 210 m and at most 350 m deep, 22 km wide, about 20 km long (see Figure 1). Tidal currents are dominated by the M_2 constituent (Heath, 1986; Vennell & Collins, 1991) as the elevation tide travels as a progressive wave around the continental shelf of Aotearoa-NZ and cause a 140° phase difference between the 150 km distance separating the limits of Greater Cook Strait (Heath, 1978). Sea surface height at both ends of a 40 km segment crossing the Narrows can be out-of-phase by 100°, and

is considered a non-divergent short channel (Vennell, 1998a, 1998b). Winds funnelled through the strait are known to be strong as it was one of a few gaps in a mountain range that spans over $\sim 1000\,\mathrm{km}$ from the centre of the North Island to the southern edge of the South Island (Vennell & Collins, 1991; Zeldis et al., 2013). While some systematic differences were found between weather stations records at the eastern and western ends of the narrows during southerlies winds, most likely caused by headland protection (Stevens, 2014), winds are predominantly along the North-South axis (Zeldis et al., 2013).

2.2 Overview of the experiment

The analysis presented here was built on observations of 1) background flow conditions from a moored acoustic doppler current profiler (ADCP), 2) wind forcing from an atmospheric weather station (AWS), 3) turbulence from an ocean microstructure glider (OMG), and model results of 4) turbulence balance terms calculated using the General Ocean Turbulence Model (GOTM) calibrated using a set of observational constraints.

Mooring and glider observations were gathered between the 23 and the 27 June, 2020 as part of Project CookieMonster (acronym for Cook strait Internal Energetics MONintoring and SynThEsis Research), using RV Kaharoa to sample north of the Cook Strait narrows, broadly representative of the Greater Cook Strait region. The mooring assembly of an upward-looking ADCP (Nortek instruments) and a SBE 37 Conductivity-Temperature-Depth sensor (CTD, SeaBird Electronics) was deployed on the seabed in the Cook Strait narrows ($174.5813°E$, $41.1651°S$) for 6 days spanning 22-27 June. The Ocean Microstructure Glider (OMG) was deployed in central Cook Strait and completed a 20 day mission, between the spanning 23 June -13 July. This study focuses on a first four day period (23-27 June) when the sampling was conducted in an area of $\sim 20\,\mathrm{km}\times 20\,\mathrm{km}$ surrounding the initial deployment site (see Figure 1). This region and period best represented wind and tidally generated turbulence, and associated vertical and horizontal interactions.

2.3 Mooring

The upward facing ADCP sampled flow velocities at 1 Hz, in 5 m bins between 35 m (surface bins unsampled due to side-lobe interference) and 295 m water depth (instrument at $\sim 15\,\mathrm{m}$ above the seabed) (Valcarcel et al., 2022). Velocities were filtered using an hourly first order low pass filter and decomposed into along and cross-strait components. Vertical shear was computed using the along and cross-strait velocity components respectively. The measurements from the CTD mounted underneath the ADCP flotation casing was used to determine the precise depth of the seabed (311.5 m). Bottom stress was calculated as:

$$\tau_b = C_d \rho_b \|U_b\|^2 \,[\mathrm{N\,m^{-2}}], \tag{5}$$

with the bottom drag coefficient $C_d \in [1 \times 10^{-3}; 2.5 \times 10^{-3}]$(Vennell, 1998a; MacKinnon & Gregg, 2005a), ρ_b and U_b the deepest measurements above the bottom boundary layer of density and speed respectively.

2.4 Ancillary measurements

Hourly atmospheric measurements from the Cape Campbell Atmospheric Weather Station, $\mathcal{O}(50\,\mathrm{km})$ away from the area of interest were included in this analysis (Valcarcel et al., 2022). Along- and cross-strait components of wind speeds at 10m from the water surface were then estimated using a Hellman power law (Hellmann, 1919; Haas et al., 2021). Wind stress was calculated as:

$$\tau_w = \rho_{air} C_d U_{10}^2 \,[\mathrm{N\,m^{-2}}], \tag{6}$$

where $\rho_{air} = 1.3\,\mathrm{kg\,m^{-3}}$ was the air density, U_{10} was the wind speed at 10 m above the surface, and the associated drag coefficient was $C_d = 1.14 \times 10^{-3}$ if $U_{10} > 10\,\mathrm{m\,s^{-1}}$ or $C_d = (0.49 + 0.065U_{10}) \times 10^{-3}$ if $U_{10} < 10\,\mathrm{m\,s^{-1}}$ (Watanabe & Hibiya, 2002). Additionally, daily averages of satellite measurements of Sea Surface Temperature (SST) produced on a 0.01° grid (JPL MUR MEaSUREs Project, 2015) were used to assess the presence of surface fronts on the path of the OMG.

2.5 Glider-based turbulent microstructure

The sampling platform was an Autonomous Underwater Vehicle (AUV) (Slocum Glider 2, Teledyne Webb), on which was mounted a MicroRider-1000EM turbulence package (MR, Rockland Scientific Instruments) and a CTD (SeaBird Electronics) (O'Callaghan & Elliott, 2022). The relatively novel Electro-magnetic (EM) sensor attached adjacently to the shear probes on the nose of the MR allowed direct measurements of flow past the sensors, and thus provided an indirect estimate of platform speed through the water. A total of 257 profiles of depth of variables of state and microstructure shear and temperature are presented here. While starting on the 24/06/2020 both upcasts and downcasts of microstructure measurements were recorded, CTD observations were only obtained during dives during the mission to save power. Unsampled salinity during climbs were determined using downsampled microstructure temperature measurements and the $T-S$ relationship from each preceding dive.

High frequency (512 Hz) measurements of the ~ 5 mm-scale orthogonal ($\partial w/\partial x$, $\partial v/\partial x$) components of velocity shear in the reference frame of the glider were gathered using the two orthogonally-mounted airfoil shear probes of the MicroRider-1000EM package (O'Callaghan & Elliott, 2022). Estimates of turbulent kinetic dissipation rates ϵ and kinematic viscosity ν were computed using the Matlab codes developed by the manufacturer (RSI Odas library version 4.3.08), following the standard technical procedure of Lueck (2016). The isotropy of turbulence was assumed (the validity of which will be revisited in the Results) and implies that, for each probe, the dissipation rate of turbulent kinetic energy ϵ can be estimated from the shear spectra following Oakey (1982):

$$\epsilon = \frac{15}{2}\nu\overline{\left(\frac{\partial u_i}{\partial x}\right)^2} = \frac{15}{2}\nu\int_0^\infty \Phi(k)dk\,[\mathrm{W\,kg^{-1}}], \tag{7}$$

where $u_i = \{v; w\}$ were the velocity components orthogonal to the path of the glider in the x coordinate. Integration of shear spectra are computed in segments of 8 s with 4 s overlap and a 2 s Fast Fourier Transform segment length, yielding 5690 ϵ estimates with on average an estimate every 0.61 m.

A major challenge with glider-based microstructure is quantification of the sensor speed through water. The EM sensor measurements permitted raw counts to be converted into physical units of shear and frequency into wave number (k) for spectral analysis. The speed at which the vehicle moves through the water U was generally computed using a flight model for the glider, given the pressure gradient and angle of attack of the vehicle (Merckelbach et al., 2010, 2019). In this study, direct EM current measurements of the speed past the sensors are used to quantify U. This has been shown to improve by 10% the accuracy of shear-based ϵ estimates, where most U differences were attributed to flow variability (Merckelbach et al., 2019), a bias presumably exacerbated in energetic flows as is the case here.

Unreliable ϵ estimates were removed from the analysis if: (1) $U < 0.2\,\mathrm{m\,s^{-1}}$ to remove internal vibrations from the inflection procedure between dives and climbs (14.8% of total points removed); (2) each probe estimate differ by an order of magnitude or more, with the greater estimate being disregarded (QC3 of Scheifele et al. (2018); 1.5% of total points removed); (3) $U < 5(\epsilon/N)^{1/2}$, that is the glider's speed is at least 5 times lower than turbulent flow velocities, suggesting that Taylor's frozen field hypothesis is invalid

(Fer et al., 2014) (QC4 of Scheifele et al. (2018); 2.3% of total estimates removed). A total of 43,300 reliable ϵ estimates are included herein.

2.6 Mixing analysis

Conservative temperature CT, absolute salinity S_A, density ρ, potential temperature θ and potential density σ_θ were computed from *in situ* measurements of temperature and practical salinity using the Gibbs SeaWater TEOS-10 formulation [1] (Ioc et al., 2010). Potential density profiles were re-ordered to be monotonically increasing with depth, and used to compute the squared buoyancy frequency squared N^2. For each profile, we identify the edges of the surface and bottom boundary mixing-layers (defining a mid-layer analogous to a weak thermocline) using a potential temperature threshold of $\Delta\theta = 0.05\,^\circ$C under the assumption that it was a reliable proxy for homogeneity within a layer (Inall et al., 2021) as: $z_{top} = z(\theta > \theta_0 - \Delta\theta)$ [m] and $z_{bottom} = z(\theta < \theta_b - \Delta\theta)$ [m] where θ_0 and θ_b were the shallowest and deepest points in the profile respectively.

The sites for the measurements of the vertical structure of the flow (ADCP), and samples of the characteristics of stratification and dissipation (OMG) were separated by 27.6 km on average (between 19.7 and 35.9 km). In order to assess the link between the vertical shear configuration, the dynamical stability of the water column and turbulent mixing generation, we consider that tidal forcing dominates the flow and allows the two datasets to be connected. Firstly, the tidal excursion length $L \equiv v_{peak}.T/\pi \in [16.5; 20.6]$km quantifies the distance over which a fluid particle travels at peak flow speed ($v_{peak} \in [1.2; 1.5]\,\mathrm{m\,s^{-1}}$) during one tidal cycle ($T \sim 12$ h), which was comparable to the average distance between sampling sites. Secondly, the observed lag between depth-averaged along-strait flow speed measured by the ADCP and the glider was on average of 37 minutes. This was more than twice yet of the same order of magnitude than the 16 min phase-lag inferred from (Vennell, 1998a), the difference arguably could be attributed to the fact that the observations presented here come from a wider section of the strait where flows were less constricted and the tidal wave travels slower. For those reasons, we assume that the vertical flow structure at the OMG mission area can be inferred from the measurements of flow velocities in the ADCP site shifted by the measured 37 min lag. Additionally, the amplitudes of depth-averaged flow velocity were different between sites, the glider measured flow speeds on average 73% of the amplitude of the ADCP measurements. Thus we use scaled magnitudes of the ADCP measured speeds to estimate bottom stress magnitudes, drag laws and GOTM mean tidal amplitudes.

Profiles of N^2 were interpolated to the ϵ and ν samples to compute the buoyancy Reynolds number that represents the intensity of turbulence (see Eq. 3). Similarly, to complement the analysis in several Discussion points, profiles of velocity shear S^2 were interpolated to match the profiles of N^2 and compute the gradient Richardson number (see Eq. 4). Time-averaged profiles of the variables of mixing relative to a normalized profile depth were displayed using the Seaborn library (Waskom, 2021) and correlation coefficients were estimated using Spearman's rank formulation (Zwillinger & Kokoska, 2000), to discuss the mean impact on turbulent mixing of wind and tidal forcing, and transient stratification in Section 4.1 and 4.2 respectively.

[1] `https://github.com/TEOS-10/GSW-Python`

2.7 1D models of turbulence

2.7.1 Law of-the-wall

Bottom (ϵ_b) and surface (ϵ_s) dissipation rates are estimated using

$$\epsilon_b = \frac{C_d^{3/2} U_{250}^3}{k z_{ab}},\ \epsilon_s = \frac{C}{kz}\left(\frac{\tau_w}{\rho_0}\right)^{3/2}\ [\mathrm{W\,kg^{-1}}], \tag{8}$$

respectively. For bottom estimates, $C_d = 2 \times 10^{-3}$ (Vennell, 1998a) is the drag coefficient, U_{250} the measurement of speed at 250 m depth (65 m away from the seabed, the first bin of average depth away from bottom influence), $k = 0.4$ Von Kármán's coefficient and z_{ab} the distance above the bottom (MacKinnon & Gregg, 2005b). For surface boundary estimates, $C = 1.76$ is an empirical scaling factor for wind-induced surface mixing (Lombardo & Gregg, 1989), $k = 0.4$ was Von Kármán's coefficient, z the depth, τ_w the wind stress (see Eq. 6) and ρ_0 the reference density at the surface (MacKinnon & Gregg, 2005b).

2.7.2 GOTM

GOTM is a one-dimensional model that computes solutions for the vertical Reynolds-Averaged Navier–Stokes equation for momentum, and temperature and salinity transport equations. A choice of closure schemes are available to calculate turbulent tracer flux Umlauf and Burchard (2005); Umlauf et al. (2012). In this application we use the two equation ($k-\epsilon$) model: solving for turbulent kinetic energy and a dissipative length scale (Canuto et al., 2001).

In order to understand general patterns of ϵ in a tidal- and wind-driven environment, there was minimal tuning of model parameters, similar to the approach for Liverpool Bay (Rippeth et al., 2001; Simpson et al., 2002; Verspecht et al., 2009). Salinity and temperature equations are solved, with a specified time-scale for relaxation to prescribed observations (interpolated to the GOTM timestep) (Rippeth et al., 2001; Simpson et al., 2002; Verspecht et al., 2009). Mean flow variables (horizontal velocity components, pressure, salinity, temperature) and turbulence variables (most notably the terms of the balance of turbulent kinetic energy equation: the rates of shear production P, buoyancy production/destruction G and dissipation ϵ) were computed over 100 evenly-spaced levels of a 193 m depth (maximum water depth in this subset of the OMG deployment) with a 10 s integration time step. Mean depth-averaged amplitudes of the dominant M2 tidal flows were used to force the external pressure gradient from tidal constituents. Air-sea interactions at the surface boundary were forced only by horizontal momentum fluxes using wind stress time series input from Eq. 6. Seabed interactions at the bottom boundary were forced with a typical bottom roughness length input that entails a hydrodynamical drag coefficient $C_D \sim 2 \times 10^{-3}$. Temperature and salinity glider profiles were interpolated to the GOTM timestep and used to force stratification.

3 Results

3.1 Background conditions

3.1.1 Tidal forcing

Flow speeds through the strait were dominated by the semi-diurnal spring tides currents, with along- and cross-strait speed components in the $\pm 1.5\,\mathrm{m\,s^{-1}}$ and $\pm 0.5\,\mathrm{m\,s^{-1}}$ ranges respectively (see panels (a)-(b) of Figure 2). Flows were dominated by the along-strait component, which axis was angled 7° from true North (not shown here). The cross-strait component presents a clear tidal signal with velocities lower by a factor of 3 compared to the along-strait component, with distinctly more variability in the vertical structure. Moreover, a phase progression of maximal along-strait axis over cross-strait axis

flow components was observed. This allowed most evidently for maximal cross-strait - eastward flows to happen during the transition from along-strait - northward to along-strait - southward peaks flows. Nevertheless, the mean vertical structure of shear was similar for both the positive and negative along-strait primary components. Herein, we focus on two flow phases of maximum and minimum bottom shear (on average $1.6\times10^{-5}\,\mathrm{s}^{-2}$ and $3.9\times10^{-6}\,\mathrm{s}^{-2}$ respectively, in the deepest 20 m of the dataset), to understand the impact of tidal flows on the mean near-bed structure of mixing (see Figure 2 (c) and Figure 4 (a)).

3.1.2 Wind forcing

Wind speeds were estimated at 10 m above the water surface through the sampling period (see panel (d) of Figure 2). An event of strong Southwesterlies funnelled through the strait was detected, with wind speeds stronger than $10.8\,\mathrm{m\,s}^{-1}$, a threshold used by Schultze et al. (2020) to characterize storm-like conditions and wind-induced surface mixing in a shallow stratified system.

3.1.3 Stratification

Density was dominated by temperature during the field experiment with occasional warming of the upper half of the water column (panels (a) and (b) of Figure 4). Here the focus was placed on analysing the variability of potential temperature θ. Weak stratification was observed through out the period with $12.5 < \theta < 14\,^{\circ}\mathrm{C}$ and top to bottom differences of $\Delta\theta < 1\,^{\circ}\mathrm{C}$ and $N^2 < 5\times10^{-5}\,\mathrm{s}^{-2}$ within a profile ($3\times10^{-9} < N^2 < 5\times10^{-5}\,\mathrm{s}^{-2}$ over the full period). Boundary limits of a weak thermocline-like mid-layer can be identified during most of the period with mid water column temperatures warmer (colder) by $\Delta\theta = 0.05\,^{\circ}\mathrm{C}$ from the reference surface (bottom) temperature, as represented by the black (red) lines in Figure 4. On average, the maximum depth of surface mixing-layer and the minimum depth of the bottom mixing-layer were 43 m and 106 m respectively. A mid-layer of 125 m and 63 m for maximum and mean thickness, respectively, was evident. At the top and bottom edges of the mid-layer the buoyancy frequency squared was on average 3×10^{-6} and $1.8\times10^{-6}\,\mathrm{s}^{-2}$ respectively, both higher by factors of 2.7 and 2.9 than the mean in the respective adjacent mixing-layer. Observations show relatively high values of $N^2 > 1\times10^{-6}\,\mathrm{s}^{-2}$ within the mid-layer limits during most of the campaign. Mean N^2 was higher in the mid-layer by factors of 2.3 and 4.1 than the mean buoyancy frequency in the surface and bottom mixing-layers, respectively. Nevertheless, episodes of quasi-homogeneity were observed, when the difference between top and bottom temperature in the profiles were less than the mid-layer delimitation threshold (dark rectangles in Figure 4), associated with relatively weak stratification with $N^2 < 1\times10^{-6}\,\mathrm{s}^{-2}$ throughout the water column.

Several occurrences of notable low density (high temperature) surface waters that extended from the surface down to ~ 100 m were observed (Figure 4(b)). The vertical extent and duration of those low density surface waters increase with each occurrence until the whole water column appears well mixed at the end of the represented time period. Pockets of relatively strong stratification $N^2 > 1\times10^{-6}\,\mathrm{s}^{-2}$ were detected at the deep edges of the low density surface waters, marked by sharp gradient of temperature-density. The last 36 h of the campaign (from the last hours of the 25^{th}) were characterized by mostly low values of $N^2 < 3\times10^{-6}\,\mathrm{s}^{-2}$ representing weak stratification and a well-mixed water column. Strengthened stratification associated with the presence of low density surface waters in the dataset caused a second peak at $N^2 \sim 1\times10^{-5}\,\mathrm{s}^{-2}$ in the distribution of buoyancy frequencies within the mid-layer (see panel (a) of Figure 4). These relatively higher temperature events were likely related to the path of the glider crossing a surface front several times, as daily averaged SST fields reveal a trend of warm surface waters from Greater Cook Strait being advected southward through the narrows (see panel (c) of Figure 3) a pattern consistent with the observations of Stevens (2014).

While the overall top to bottom density gradients were weak (differences of the order of $0.05\,\mathrm{kg\,m^{-3}}$), N^2 levels in the mid-layer (i.e. the deep edge of the low density surface waters) were up to 2 orders of magnitude larger than in the surface and bottom mixing-layers.

3.2 Turbulence

3.2.1 Dissipation rates

Evolution of the rate of dissipation of turbulent kinetic energy ϵ for four days is shown in Figure 4(c). There was evidence of the intensification of surface mixing within the upper $\sim 50\,\mathrm{m}$, mostly confined to the surface mixing-layer (defined above). Elevated values of TKE dissipation rates predominantly $> 1{\times}10^{-7}\,\mathrm{W\,kg^{-1}}$ were observed within the surface layer, and high dissipation rates of $\epsilon > 1\times10^{-6}\,\mathrm{W\,kg^{-1}}$ were also episodically detected in the first 10 m. Bottom-driven turbulent mixing pulses that follow the semi-diurnal tidal $\sim$ 6 h frequency were also observed. Predominantly, these ascending patches of elevated dissipation with $1{\times}10^{-7} < \epsilon < 1{\times}10^{-4}\,\mathrm{W\,kg^{-1}}$ originate from the seabed and propagate upward in the water column, mostly within the bottom mixing-layer extending up to 75 m from the seabed. In the mid-layer lower levels of dissipation were observed, however with several episodes of elevated values of dissipation ($1{\times}10^{-7} < \epsilon < 1\times10^{-6}\,\mathrm{W\,kg^{-1}}$). The definition of the layer breaks down during most of those episodes, and low levels of buoyancy frequency, a high degree of temperature homogeneity and relatively high values of dissipation are observed throughout the water column (see black rectangles in Figure 4).

3.2.2 Mixing parameters

Intense turbulence as quantified using the buoyancy Reynolds number Re_b, the ratio of energy dissipation ϵ and the strength of stratification N^2 (see Eq. 3), as shown in panel (d) of Figure 4. Values spanning over 8 orders of magnitude were measured, with $2 < Re_b < 7{\times}10^8$ indicating intense turbulence mixing. Scenarios where (i) low dissipation rates overcoming a very weak stratification background or (ii) strong dissipation overpowering a relatively strong stratification strength produce intense turbulence. Several periods of more than 3 hours of fully turbulent water column with $Re_b > 10^4$ were observed, with 4 instances matching the weakly stratified - relatively high dissipation episodes when a mid-layer was not detected anymore. 74% of the dataset was characterized by $Re_b > 1\times10^4$ with 80 very high values of $Re_b > 10^7$ also detected, from both bottom and surface driven mixing. Out of those periods, the mid-layer region was mainly characterized by relatively low intensity with 84% of $Re_b < 10^5$.

Elevated levels of vertical diffusivity of mass K_z, computed using Eq. 2 the Osborn (1980) formula with a constant coefficient for the efficiency of mixing $R_f/(1-R_f) = 0.2$ (i.e. $R_f = 0.17$), were observed throughout the dataset (see panel (f) of Figure 4). Because ν the kinematic viscosity of seawater was almost constant ($\nu \in [1.2; 1.3]{\times}10^{-6}\mathrm{m^2\,s^{-1}}$), K_z was proportional to Re_b by a factor of $\sim 2.5{\times}10^{-7}$ and thus also shares the same features of variability. While portions of the mid-layer show moderate levels of diapycnal diffusivity and K_z can be as low as $8.2\times10^{-7}\,\mathrm{m^2\,s^{-1}}$, 92% of the dataset was in a regime of vertical diffusivity an order of magnitude or more higher than $3{\times}10^{-5}\,\mathrm{m^2\,s^{-1}}$, the global average for the upper 1000 m of the ocean (Waterhouse et al., 2014). Highest ϵ values were found near the seabed, where the elevated pulses of ϵ were met with very weak levels of stratification.

Weak stratification ($Ri_g^{-1} > 1$) and conditions for shear instability ($Ri_g^{-1} > 4$) were observed (Figure 4(g)). 52% of observations were weakly stratified and 35% were greater than the critical value of 4 for shear instability. Most super-critical values were

detected near the seabed but small subsets were also detected higher up in the water column, as high as 35.5 m below the surface.

3.2.3 Vertical structure of mixing

The levels of dissipation were observed to vary by over 7 orders of magnitude between 2.3×10^{-11} and $2.7 \times 10^{-5}\,\mathrm{W\,kg^{-1}}$. Around 70% of measurements were above $1 \times 10^{-8}\,\mathrm{W\,kg^{-1}}$ indicating relatively strong levels of energy dissipation for a coastal system (Figure 5(a)-(b)). On average, ϵ decreased by more than one order of magnitude between the surface mixing-layer and the top of the mid-layer, with the sharpest decrease observed in the first 10% of the water column (Figure 5(a)). Similarly, dissipation rates decrease with distance from the seabed in the bottom mixing-layer, by more than one order of magnitude between deepest and shallowest depths. Overall dissipation values are similarly distributed between surface and bottom mixing-layers, with $\hat{\epsilon}$ of $2.9{\times}10^{-8}\,\mathrm{W\,kg^{-1}}$ and $3.8 \times 10^{-8}\,\mathrm{W\,kg^{-1}}$ respectively, and 26% and 27% number of samples of $\epsilon > 1 \times 10^{-7}\,\mathrm{W\,kg^{-1}}$ respectively (Figure 5(b)). Relatively lower levels of dissipation were observed in the mid-layer with 89% of values below $1{\times}10^{-7}\,\mathrm{W\,kg^{-1}}$ and a mean of $1.1{\times}10^{-8}\,\mathrm{W\,kg^{-1}}$, 2.7 to 3.5 times lower than the surface and bottom mixing-layers mean values respectively, with depth average values decreasing only minimally with depth.

Differences in behaviour of the buoyancy frequency squared within each layer were highlighted in averaged profiles and distributions in panels (c)-(d) of Figure 5. The surface layer exhibited a relatively stable configuration with values oscillating around a mean of $N^2 = 3.6 \times 10^{-7}\,\mathrm{s^{-2}}$, outside a sharp increase towards the surface with relatively high first percents of the normalized water column. The bottom layer was characterized by more variability with depth and a narrower distribution of values around a lower mean of $2.7{\times}10^{-7}\,\mathrm{s^{-2}}$. The mid-layer was characterized by a wider distribution with two peaks around a mean of $8.4{\times}10^{-7}\,\mathrm{s^{-2}}$, 2.4 and 3.1 times higher than in the surface and bottom mixing-layers respectively.

The intensity of turbulence reflects the ratio of the evolution with depth of dissipation and buoyancy frequency squared (Eq 3). The first and last 25% of the water column exhibit high values with mean $Re_b > 5 \times 10^4$ (Figure 5(e)). Re_b decreases by almost an order of magnitude from each mixing-layer to a mean of $1.1{\times}10^4$ in the mid-layer. Interestingly, elevated average values of N^2 near the boundaries attenuate the steep increase of dissipation towards the limit, so that the trend reverses for a few percents of the water depth near each boundary. While distributions in both mixing-layers are similarly log-normal, the mean in the bottom layer of 1.2×10^5 is 1.73 higher than in the surface layer, reflecting the larger number of $Re_b > 10^5$ samples in the bottom layer where notably lower levels of N^2 were detected (Figure 5(f)). Both layers show much higher numbers of samples of intense mixing with $Re_b > 10^5$ (44% and 53% of points in the surface and bottom mixing layer respectively) than in the mid-layer (16%). Additionally, while 98.9% of total samples were $Re_b < 1 \times 10^2$, a larger number of values $< 1{\times}10^2$ were observed within this layer (2.7% of samples compared to 0.4% and none in the surface and bottom layers respectively).

3.3 Comparison with modelled turbulence distributions

Elevated dissipation rates were observed in the surface and bottom mixing-layers (Figure 5(a)). Comparisons to one-dimensional water column models of steady boundary stress -driven dissipation (the law of-the-wall) and of the transport equations of momentum, salt and heat with resolved turbulent fluxes (GOTM) were undertaken in order to evaluate relative roles and scales.

3.3.1 Law of the wall

Temporal variability of elevated near-bed dissipation rates was well represented by one-dimensional models. However, differences in magnitude and vertical variability were observed (Figure 6(a)-(b)). While the deepest estimates were within one or two orders of magnitude of the observed rates, the rate at which ϵ decreases away from the boundary was underestimated by 1D models. Notably, the upward plume-like propagation of dissipation described in Section 3.2.1, a characteristic feature of the bottom mixing-layer observations is absent in the steady model. Furthermore, the law overestimates dissipation rates almost everywhere in the surface layer, as shown in panels (a)-(b) of Figure 6). Both the magnitudes and rate at which ϵ decreases with depth were overestimated, except for the weakest winds periods in the dataset (for example, when the wind speed was less than $5\,\mathrm{m\,s^{-1}}$ at the beginning of the sampling window before 2pm on the 23 and between 11am and 1pm on the 26, see Figure 2(d)). Very high values of ϵ ($> 1{\times}10^{-5}\,\mathrm{W\,kg^{-1}}$) were estimated for the first few percents of the normalized water column, which matches some of the observed surface values. Interestingly, elevated wind-driven dissipation rates from the law extend outside of the observed high wind period.

3.3.2 GOTM

GOTM estimates of dissipation rate compared reasonably well with observed magnitudes and variability of ϵ (Figure 6(a)&(c)). Broadly, surface-driven dissipation was within an order of magnitude of the observed ϵ. The exception was during the weak winds forcing in the strait (e.g. 23 June) where surface points are systematically overestimated by the model. Bottom-driven dissipation was also within two orders of magnitude of observed ϵ. Largest differences were typically observed near the seabed outside of the pulses of elevated rates. The upward propagation of dissipation was qualitatively well represented, which was a clear improvement from the steady state depiction by the law of-the-wall. The connection in the middle of the water column of surface and bottom driven turbulence was the least well described feature of the observations, the vertical extent of the elevated surface and bottom driven mixing envelopes were mostly underestimated, with much lower estimates observed in the middle of the water column. This was most evident during the periods of water column homogeneity marked by the black rectangles, where the estimates show a separation between surface and bottom driven elevated dissipation that was not observed in the measurements.

4 Discussion

Turbulence in a weakly-stratified, energetic strait was examined using autonomous profiling observations and a one-dimensional model of turbulent kinetic energy transport. The intersection of tidally and wind -driven turbulence resulted in high levels of dissipation and weak stratification within boundary mixing layers, separated by a relatively less active mid-layer. In order to quantify the impact of background conditions on the vertical structure of turbulence as well as the differences between observations and model outcomes to study the processes involved in production/destruction of TKE, we analyse subsets of time-averaged data using thresholds on tidally-driven bottom shear, wind speed and surface density variability (Figure 4(a)).

4.1 How do the surface and bottom mixing-layers compare with one-dimensional paradigms?

4.1.1 Tidally driven mixing

Evidence of the interaction of tidal flows with the seabed, associated with bottom drag and enhanced vertical shear, driving TKE dissipation in the bottom mixing-layer is shown in Figure 7(a)&(c) and Figure 9. Maximum shear regime drive weaker ϵ aver-

age levels than the minimum shear regime in the shallower portion of the bottom layer ($0.5 < \hat{z} < 0.6$), increasing by an order of magnitude to $\epsilon = 2.2 \times 10^{-7}\,\mathrm{W\,kg^{-1}}$ (3.4 times higher than for the minimum shear regime) in the deepest depth averages ($\hat{z} > 0.9$). This further represents the pulses of upward propagation of TKE and subsequent dissipation, an expected feature in tidally forced bottom mixing-layers (Schultze et al., 2017, 2020). The sevenfold increase in the number of $\epsilon > 1 \times 10^{-6}\,\mathrm{W\,kg^{-1}}$ values observed in the maximum versus minimum shear regimes may provide further indication of the detection of low-maturity dissipation events (Smyth et al., 2002; Gregg et al., 2017). Strong rank correlation (> 0.5) between shear or bottom stress and dissipation rates where $\hat{z} > 0.85$ or > 0.9 respectively, consistent with MacKinnon and Gregg (2005b), is additional evidence of turbulence enhancement from flow-seabed interaction.

GOTM overestimates average dissipation in the bottom boundary-layer by up to an order of magnitude in either regime, however GOTM ϵ are within one standard deviation of the observations (Figure 7(a)). As noted, GOTM reproduces the upward propagation of the bottom dissipation pulses, which appears in the crossing of the regime averaged ϵ profiles. The average depth at which this happens was 7% deeper in the water column in the model estimates, suggesting that the speed at which TKE propagates upward and dissipates was underestimated by the model. Modelled shear production of TKE P seems to be the major source of TKE in either shear regime in the deepest points of the layer ($\hat{z} > 0.75$), as P/ϵ ratios are on average 34 (16) and 30 (11) higher than G/ϵ for observed and modelled ϵ respectively in the maximum (minimum) shear regime (Figure 7(b)-(c)). This suggests that convective motions is not playing a major role in the tidal cycle of stratification and dissipation through buoyancy production of TKE in our observations (Simpson et al., 2002). Interestingly, the depth away from the seabed at which P becomes lower in the maximum versus minimum shear regime (i.e. the indication of the rate at which pulses propagate upward in the water column) is higher than for modelled ϵ, further indicating that the vertical transport of TKE is underestimated in the model. Model underestimates of energy dissipation can impact the accurate representation of vertical fluxes within the bottom mixing-layer, having documented implications for nutrient transport in stratified shelf seas subsurface (Becherer et al., 2022).

4.1.2 Wind driven mixing

Wind stress drives substantial mixing in the upper half of the water column, down to the bottom mixing-layer (Figure 8(a)). High winds induce elevated dissipation rates in the surface mixing layer, with higher average by an order of magnitude and 20 times more numerous values of $\epsilon > 1 \times 10^{-6}\,\mathrm{W\,kg^{-1}}$ (Figure 8(c)). A significant shift in distributions between high and low winds is also observed in the middle (surface) layer, with 2 (4) times higher mean ϵ. Schultze et al. (2020) observed a consistent increase during a storm (wind speeds $> 10.8\,\mathrm{m\,s^{-1}}$) of similar duration ($\sim 2$ days) in a ~ 4 times shallower shelf sea water column, associated with an overall 67% increase in surface mixed layer chlorophyll-a fluorescence. Although the enhanced thermocline turbulence was forced by $\sim 25\%$ faster maximal winds and resulted in 5 times higher mean ϵ, their study suggests a comparable impact on chlorophyll-a transport and primary production in our system. Additionally, observed ϵ were strongly (> 0.5) and moderately (> 0.3) correlated to wind stress in the surface mixing-layer, in the first 15% and 20% of the normalized water column, respectively (see panel (d) of Figure 8). This is consistent with MacKinnon and Gregg (2005b) even though the sampled water column was 50% shallower in our study and with the caveat that our observations only span one high winds event.

Average GOTM ϵ estimates were in agreement with the glider ϵ and, within a standard deviation through the surface mixing-layer and parts of the mid-layer for both wind regimes (Figure 8(a)). Disagreements between observed and modelled $\hat{\epsilon}$ were found from the surface down to the first half of the average mid-layer ($\hat{z} < 0.35$), where GOTM underestimates dissipation by up to an order of magnitude for the low winds regime. How-

ever, while GOTM underestimates weak wind-stress driven dissipation everywhere in the surface mixing-layer but the shallowest percents, GOTM overestimates dissipation in the strong wind tress regime down to 3/4 of the surface mixing-layer. Shear production is strongly > 0.5 correlated to observed dissipation in the first 2/3 of the surface mixing-layer (Figure 9), which echoes the very similar means and distributions observed between both variables in the high winds regime, and the differences present in the last third of the layer (Figure 8). Interestingly, in the weak winds regimes for $\hat{z} > 0.15$ in the layer, P is higher by up to an order of magnitude than modelled ϵ while buoyancy production ($G > 0$) and destruction ($G < 0$) are only 6 and 2 times lower on average than P, suggesting a more important role for convective-driven turbulence and re-stratification in the layer than in the bottom mixing-layer.

4.1.3 Influence of horizontal gradients on the vertical structure of mixing

The vertical structure of P estimates matches the vertical structure of observed ϵ in both boundary mixing-layers, and buoyancy production plays a relatively minor role (Figure 7-8). Depth averaged dissipation rates from observations and model output are within ± 0.4 and ± 0.3 orders of magnitude of modelled total production (P+G) respectively, suggesting relative steady balance between production and dissipation (Figure 10), the hypothesis used to formulate Eq. 2 (Osborn, 1980; Gregg et al., 2017; Polzin & McDougall, 2022). To note here, the average contribution of G through production ($G > 0$) and destruction ($G < 0$) of TKE varies with depth and affects each layer differently (Figure 10). While $G > 0$ in the larger portions of both surface and bottom mixing-layers, two depth bins at the base of the surface mixing-layer show elevated negative G values, potentially linked to the observed $G < 0$ in the mid-layer. Furthermore, most of the observed dissipation in the water column is lower that total production while the deepest levels of the surface mixing-layer and the shallowest levels of the mid-layer show observed dissipation higher that total production. This pattern is not present with the modelled ϵ where viscous and turbulent vertical transport is resolved, indicating 3D complexity not represented in a 1D model.

The influence of submesoscale horizontal variability in Greater Cook Strait on boundary mixing layer interactions in the vertical can be discussed. Evidence of a SST front advected ~ 40 km south during 25-27 June is shown here (Figure 3). Furthermore, at the submesoscale in Greater Cook Strait, surface mixed layer baroclinic instabilities and fronts of typical length scale $0.1 - 1.6$ km can have an advection timescale of $0.2 - 8$h (Jhugroo et al., 2020), comparable to the 6h period of tidal generation of bottom boundary layer in a strait. These features have been shown to strengthen vertical stratification to $\mathcal{O}(1{\times}10^{-4}\,\mathrm{s}^{-2})$, reduce mixed-layer depth and decrease diapycnal mixing (Jhugroo et al., 2020). Moreover, the interaction of surface momentum fluxes and horizontal gradients can affect advection patterns in Greater Cook Strait (Jhugroo et al., 2020) and wind-driven mixing through wind straining in broadly similar systems (Verspecht et al., 2009). To note, static approximations of large scale horizontal gradients of $\theta{-}S_A$ can be prescribed to GOTM and notably analyse the impact of tidal straining on the stratification cycle (Rippeth et al., 2001; Simpson et al., 2002). Nevertheless, the choice has been made here to not prescribe static gradients, as they would fail to represent the documented higher degree of variability of horizontal gradients in Cook Strait (Stevens, 2014, 2018; Jhugroo et al., 2020).

4.2 Does the stratification in the mid water column act as a vertical barrier to mixing?

Mean flows in Cook Strait have been described as weakly stratified (Stevens, 2014, 2018), however, transient stratification can inhibit turbulence-driven mixing in the mid water column and isolate surface from bottom driven diapycnal mixing (Figure 11). For

$0.25 < \hat{z} < 0.8$, while ϵ was 1.7 times weaker, N^2 was 4.2 stronger, translating to 7.3 times weaker K_z low density surface waters events. The largest difference was at the average interface depth between bottom mixing-layer and mid-layer ($\hat{z} \sim 0.5$) with 15.7 times lower diffusivity. GOTM results show the role of the base of the surface layer and the major portion of the mid-layer where G negatively affects total production and destroys turbulence (Figure 10). Becherer et al. (2022) similarly observe $G < 0$ at the base of the pycnocline (i.e. a relatively different definition for a mid-layer) and highlight the combined roles of P and vertical transport of TKE to balance observed dissipation rates. Moreover, 18.1 times more elevated buoyancy destruction of TKE ($G < 0$) balancing P estimates of the same order $\sim 3 \times 10^{-10}\,\mathrm{W\,kg^{-1}}$ inside a LDSW as opposed to outside where P outweighs $G < 0$ by a factor of 4 (not shown here). This highlights the insulating role of transient stratification, as full water column intense mixing ($Re_b > 1 \times 10^4$) and dynamical instability ($Ri_g^{-1} > 4$) throughout the mid water column are only evident outside the episodes of strengthened mid water column stratification. Conspicuously, on three occasions (first three black rectangles in Figure 4) the mid-layer definition breaks down and each boundary-driven mixing entrains TKE in the relatively weakly stratified mid water column and sustains diapycnal mixing. Transient stratification in Cook Strait thus affects the vertical transport of TKE generated in the bottom and surface mixing-layers into the mid-layer. It is thus likely to have an unexpected, major impact on local diffusive fluxes of mass and arguably of trace gases (Peeters et al., 1995), suspended sediments (Zulberti et al., 2020) and nutrients (Williams et al., 2013; Becherer et al., 2022) across isopycnals.

Transient stratification from the intensified gradients of density associated with the presence of low density surface waters stabilizes the mean flow, and is coupled with reduced dissipation rates and turbulence intensity (Figure 12). Median (mean) Ri_g^{-1} is reduced by a factor of 4 (3.5) and thus becomes sub-critical when LDSW are detected compared to when they are not. Jointly, median (mean) turbulence intensity is reduced by a factor of 2.4 (2.6), with similar power-law fits of $Ri_g^{-1} = 0.017 Re_b^{0.52}$ and $Ri_g^{-1} = 0.004 Re_b^{0.6}$ for samples outside or inside a LDSW event, respectively. Moreover, in the mid-layer, a small subset of samples show low intensity levels with $Re_b < 1 \times 10^2$, indicating anisotropic mixing (Shih et al., 2005; Smyth et al., 2002), see Figure 5 and Section 3.2.3. The small number of anisotropic turbulence samples supports the hypothesis for Eq. 7, however their presence suggests that fluid particles in the mid-layer were in the transitional regime, in which turbulence was not fully isotropic but was active enough to mix stratification (Schultze et al., 2017; Bouffard & Boegman, 2013; Shih et al., 2005). 5−20% of those points were even indicative of quiescent flow, where $Re_b < 7 - 20$ and turbulence activity does not induce diapycnal mixing (Schultze et al., 2017). Further to the point of the stabilizing role that the mid-layer can play with transient stratification, 97% of subcritical and low intensity samples are observed during the presence of a LDSW (Figure 12). Nevertheless, 49% and 26% of overall samples in the thermocline-like mid-layer indicate weak stratification ($Ri_g^{-1} > 1$) and dynamical instability ($Ri_g^{-1} > 4$) respectively, with average $Ri_g^{-1} = 2$, twice the mean in Rippeth et al. (2009) where the authors argue for the importance of intermittently-measured shear spikes and associated dynamical instability in enhancing mixing and nitrate fluxes across the thermocline.

4.3 Do dynamical instability and critical mixing efficiency drive elevated dissipation rates?

Supercritical values of observed dynamical stability and modelled mixing efficiency are associated with observations of elevated dissipation rates (Figure 13). Modelled flux Richardson numbers as $R_f \equiv -G/P$ are calculated here considering only negative values of G, with $G \equiv < w'b' >$, the averaged product of vertical velocity and buoyancy fluctuations (Umlauf et al., 2012). $G > 0$ (i.e. w' and b' are positively correlated) represents naturally-occurring convection and the conversion of potential energy to kinetic energy. Oppositely, $G < 0$ (i.e. w' and b' are negatively correlated) represents the rate

at which stratification taxes turbulence (Caulfield, 2020). Considering only $G < 0$, thus a sum of irreversible (i.e. sign-definite) mixing rates and reversible (i.e. sign-indefinite, but here sign-constrained) stirring rates, allows to exclusively represent one-way exchanges between kinetic and potential energy reservoirs (Winters et al., 1995; Salehipour & Peltier, 2015; Caulfield, 2020). Equi-partitioned sub-ensembles of ϵ values are used to highlight transitional states of flow stability and mixing efficiency (Figure 13). Increasing sub-ensemble levels of ϵ are detected with increasing levels of Ri_g^{-1} and R_f^{-1}, with median (mean) values associated with ϵ_{low} and ϵ_{high} levels increasing by factors of 2.4 (2.4) and 2.2 (3), respectively. Regression lines show laws of $Ri_g = \beta R_f^{\alpha}$ with $\beta \in [0.4; 0.5]$ and increasing $\alpha = \{0.1; 0.2; 0.4\}$ for the increasing ϵ intervals, potentially supporting the hypothesis that flow instability sets the upper bound of mixing efficiency (Holleman et al., 2016). The median values are characterized by a law of $Ri_g = 1.6R_f^{1.1}$ which represent well weak stratification with $Ri_g \sim R_f$ and a turbulent Prandtl number $Pr_t = 1.6 \sim 1$, suggesting similar mixing for heat and momentum (Smyth et al., 2019; Caulfield, 2020). Interestingly, the most common ϵ conditions (ϵ_{mid} in this study) are associated with a median value of $R_f = 0.17$, giving further statistical support for using the canonical mixing efficiency coefficients for "average" turbulence conditions (Osborn, 1980; Gregg et al., 2017). Furthermore, the increasing ϵ intervals show statistical transitions between the observed states of low dissipation rates from dynamically stable flow ($Ri_g > 1/4$) and decaying turbulence ($R_f > 0.17$), to average ϵ from near-critical stability ($Ri_g = 0.22 \sim 1/4$) and efficiency ($R_f = 0.17$), to elevated ϵ from unstable flow ($Ri_g < 1/4$) and growing turbulence ($R_f < 0.17$) (Smyth et al., 2019).

4.4 How does the mixing observed in Cook Strait compare with observations from similar systems?

Depth-averaged turbulence intensity and vertical diffusivity were up to an order of magnitude higher in Cook Strait than in Gibraltar strait (Wesson & Gregg, 1994), the canonical strait at this scale (Stevens, 2018). Indeed, depth-averaged dissipation rates in this portion of Cook Strait were comparable, within a factor of 3, to Gibraltar levels while N^2 depth-averages can be three orders of magnitude lower. When comparing overall ranges, the levels of mixing presented here can be up to three orders of magnitude higher than in tidal channels of varied constrictional width and depths forced by similar tidal flow speeds (Alford et al., 2011; Tanaka et al., 2014; Itoh et al., 2010). While Itoh et al. (2010) report similar levels of shear, stratification and thus Ri_g^{-1} to Cook Strait, the sampled water column was almost four times deeper and ϵ maxima only reach $1 \times 10^{-6}\,\mathrm{W\,kg^{-1}}$. Methodological biases can obscure the comparisons with other systems, especially with the aforementioned studies which measured turbulence with vertical profilers which fail to capture near-surface waters and are by design limited in their sampling in space and time. This emphasizes how autonomous platforms offer a methodological pathway to better sample boundary layers and capture the sporadic very high levels of dissipation associated with the initial stages of wave breaking and turbulence onset (Smyth et al., 2002).

Extensive autonomous sampling of turbulence in a broadly similar shelf sea environment of the North Sea off the coast of Germany, revealed a comparable range of elevated dissipation rates with $\epsilon \in [1 \times 10^{-11}; 1 \times 10^{-5}[\,\mathrm{W\,kg^{-1}}$ in a ~ 4 times shallower and averaged N^2 higher by up to three orders of magnitude than in this present work (Schultze et al., 2017). Although their measurements showed average dissipation rates twice as high in the thermocline layer (2−3 times higher for the whole water column), the much stronger stratification ($1 \times 10^{-3} < \overline{N^2} < 1 \times 10^{-2}\,\mathrm{s^{-2}}$ and most bulk Ri samples > 1) resulted in notably different distributions of turbulence intensity. Indeed, 6% of measurements showed isotropic turbulence in the thermocline layer (69−81% for the full water column) compared to 97.3% (98.9%) in this study (see Section 3.2.3), reiterating the role of mid water column stratification in dampening turbulence and insulating surface and bottom mixing layers. Furthermore, similarly to this study, storm

conditions have been shown to increase ϵ by an order of magnitude in both surface and thermocline layers, highlighting periods of marginal stability (bulk $Ri < 1$) and rapid homogenization of the water column (Schultze et al., 2020). Moreover, when compared to GOTM results, extensive OMG measurements demonstrate the importance of shear instabilities on the entrainment of nutrients from the bottom mixed layer into the pycnocline (Becherer et al., 2022), further emphasizing the importance of studying the interplay between turbulence-driven mixing layers in shelf sea systems.

5 Concluding remarks

Observations of enhanced bottom tidally-driven shear and strong surface wind stress are combined with *in situ* Ocean Microstructure Glider (OMG) measurements of background stratification and dissipation rates to report on elevated turbulence in relatively well defined boundary mixing-layers. Large-scale advection of low density surface waters through the strait provide transient stratification that intermittently stabilizes an otherwise weakly stratified mid water column, and weakens turbulence intensity and diapycnal mixing. One-dimensional model results of the partition of turbulent kinetic energy balance terms allow to identify the mechanisms influencing the observed vertical structure of mixing. Observed dissipation rates compare well with modelled total production of TKE and elevated values in the boundary mixing layers are predominantly related to enhanced shear production of TKE, while transient stratification in the mid water column is linked to buoyancy destruction (negative production) of TKE. Furthermore, the statistics of increasing dissipation rates levels are contextualized in the framework of critical transitions towards states of dynamical instability of the mean flow and mixing efficiency allowing for turbulence growth.

Here we present a sizable dataset of $43,300$ measurements of elevated turbulence from an ocean glider, among the largest obtained to date. This work showcases the value of autonomous sampling platforms to capture intermittent mixing processes and characterize the vertical structure of mixing in shelf seas. When combined to one-dimensional models of turbulence, albeit neglecting horizontal variability notably from submesoscale scalar gradients, these measurements have improved understanding of the intersections between turbulent kinetic energy balance and observations of dynamical stability, turbulence intensity and diapycnal diffusivity. The broad range of turbulence parameters in this energetic weakly-stratified system is promising to scrutinize the variability of the efficiency of turbulent mixing in future works. Finally, as revealed by continuous sampling, the interplay of boundary-influenced mixing layers regulates diffusive fluxes in the coastal ocean, influencing local primary productivity and air-sea interactions with far-reaching implications for Earth's climate.

6 Acknowledgements

We acknowledge funding for Project CookieMonster by the Royal Society Te Apārangi Marsden Fund (NIW1702) and the NIWA capex investment programme, deployments oversight by Fiona Elliott and Brett Grant and assistance from the crew of RV Kaharoa. We also acknowledge technical support from Rockland Scientific to process the OMG data, specifically from Justine McMillan and Evan Cervelli. Wind and flow speeds (Valcarcel et al., 2022) and ocean microstructure glider (O'Callaghan & Elliott, 2022) datasets are open access. GOTM versions, test cases and documentation are available at https://gotm.net.

References

Aikman, F. (1984, January). Pycnocline development and its consequences in the Middle Atlantic Bight. *Journal of Geophysical Research*, *89*(C1), 685-694.
Alford, M. H., Mackinnon, J. A., Nash, J. D., Simmons, H., Pickering, A., Klymak,

J. M., ... Lu, C. W. (2011). Energy flux and dissipation in luzon strait: Two tales of two ridges. *Journal of Physical Oceanography*, *41*(11), 2211–2222. doi: 10.1175/JPO-D-11-073.1

Becherer, J., Burchard, H., Carpenter, J. R., Graewe, U., & Merckelbach, L. M. (2022). The role of turbulence in fueling the subsurface chlorophyll maximum in tidally dominated shelf seas. *Journal of Geophysical Research*, (Submitted).

Bianchi, A. A., Bianucci, L., Piola, A. R., Pino, D. R., Schloss, I., Poisson, A., & Balestrini, C. F. (2005). Vertical stratification and air-sea CO2 fluxes in the Patagonian shelf. *Journal of Geophysical Research C: Oceans*, *110*(7), 1–10. doi: 10.1029/2004JC002488

Borges, A. V., Delille, B., & Frankignoulle, M. (2005). Budgeting sinks and sources of CO2 in the coastal ocean: Diversity of ecosystem counts. *Geophysical Research Letters*, *32*(14), 1–4. doi: 10.1029/2005GL023053

Bouffard, D., & Boegman, L. (2013). A diapycnal diffusivity model for stratified environmental flows. *Dynamics of Atmospheres and Oceans*. doi: 10.1016/j.dynatmoce.2013.02.002

Cacchione, D. A., Pratson, L. F., & Ogston, A. S. (2002). The shaping of continental slopes by internal tides. *Science*, *296*(5568), 724-727.

Canuto, V. M., Howard, A., Cheng, Y., & Dubovikov, M. S. (2001). Ocean turbulence. Part I: One-point closure model-momentum and heat vertical diffusivities. *Journal of Physical Oceanography*, *31*(6), 1413–1426. doi: 10.1175/1520-0485(2001)031⟨1413:OTPIOP⟩2.0.CO;2

Caulfield, C.-c. P. (2020). Open questions in turbulent stratified mixing : Do we even know what we do not know ? *Physical Review Fluids*, *5*(11), 110518. doi: 10.1103/PhysRevFluids.5.110518

Chiswell, S. M., Zeldis, J. R., Hadfield, M. G., & Pinkerton, M. H. (2017). Wind-driven upwelling and surface chlorophyll blooms in Greater Cook Strait. *New Zealand Journal of Marine and Freshwater Research*, *51*(4), 465–489. doi: 10.1080/00288330.2016.1260606

Fer, I., Peterson, A. K., & Ullgren, J. E. (2014). Microstructure measurements from an underwater glider in the turbulent Faroe Bank Channel overflow. *Journal of Atmospheric and Oceanic Technology*, *31*(5), 1128–1150. doi: 10.1175/JTECH-D-13-00221.1

Gregg, M. C., D'asaro, E. A., Riley, J. J., & Kunze, E. (2017). Mixing Efficiency in the Ocean.
doi: 10.1146/annurev-marine-121916

Haas, S., Krien, U., Schachler, B., Bot, S., kyri petrou, Zeli, V., ... Bosch, S. (2021). wind-python/windpowerlib: Silent Improvements (v0.2.1).
doi: 10.5281/zenodo.4591809

Heath, R. A. (1978). Semi-diurnal tides in cook strait. *New Zealand Journal of Marine and Freshwater Research*, *12*(2), 87–97. doi: 10.1080/00288330.1978.9515730

Heath, R. A. (1986). In which direction is the mean flow through Cook Strait, New Zealand — evidence of 1 to 4 week variability? *New Zealand Journal of Marine and Freshwater Research*, *20*(1), 119–137. doi: 10.1080/00288330.1986.9516136

Hellmann, G. (1919). Über die Bewegung der Luft in den untersten Schichten der Atmosphäre, Kgl.

Holleman, R. C., Geyer, W. R., & Ralston, D. K. (2016). Stratified Turbulence and Mixing Efficiency in a Salt Wedge Estuary. *Journal of Physical Oceanography*, *46*(6), 1769–1783. doi: 10.1175/jpo-d-15-0193.1

Inall, M. E., Toberman, M., Polton, J. A., Palmer, M. R., Mattias Green, J., & Rippeth, T. P. (2021). Shelf seas baroclinic energy loss: * pycnocline mixing and bottom boundary layer dissipation. *Journal of Geophysical Research: Oceans*. doi: 10.1029/2020jc016528

Ioc, Scor, & Iapso. (2010). The international thermodynamic equation of seawater – 2010: Calculation and use of thermodynamic properties. *Intergovernmental Oceanographic Commission, Manuals and Guides No. 56*(June), 196.

Itoh, S., Yasuda, I., Nakatsuka, T., Nishioka, J., & Volkov, Y. N. (2010). Fine- and microstructure observations in the Urup Strait, Kuril Islands, during August 2006. *Journal of Geophysical Research: Oceans*, *115*(8), 1–12. doi: 10.1029/2009JC005629

Jhugroo, K., O'Callaghan, J., Stevens, C. L., Macdonald, H. S., Elliott, F., & Hadfield, M. G. (2020). Spatial Structure of Low Salinity Submesoscale Features and Their Interactions With a Coastal Current. *Frontiers in Marine Science*, *7*(October). doi: 10.3389/fmars.2020.557360

Jones, C., Creed, E. L., Glenn, S., Kerfoot, J., Kohut, J., Mudgal, C., & Schofield, O. (2005). Slocum Gliders - A Component of Operational Oceanography. *Autonomous Undersea Systems Institute Symposium Proceedings*.

JPL MUR MEaSUREs Project. (2015). GHRSST Level 4 MUR Global Foundation Sea Surface Temperature Analysis. Ver. 4.1. doi: 10.5067/GHGMR-4FJ04

Lombardo, C. P., & Gregg, M. C. (1989). Similarity scaling of viscous and thermal dissipation in a convecting surface boundary layer. *Journal of Geophysical Research: Oceans*, *94*(C5), 6273-6284. doi: 10.1029/JC094iC05p06273

Lucas, N. A., Grant, A. L., Rippeth, T. P., Polton, J. A., Palmer, M. R., Brannigan, L., & Belcher, S. E. (2019). Evolution of oceanic near-surface stratification in response to an autumn storm. *Journal of Physical Oceanography*, *49*(11), 2961–2978. doi: 10.1175/JPO-D-19-0007.1

Lueck. (2016). RSI Technical Note 028: Calculating the rate of dissipation of turbulent kinetic energy. , 18.

Lueck, R. (2002). *Oceanic Velocity Microstructure Measurements in the 20th Century.*

MacKinnon, J. A., & Gregg, M. C. (2005a). Near-inertial waves on the New England shelf: The role of evolving stratification, turbulent dissipation, and bottom drag. *Journal of Physical Oceanography*, *35*(12), 2408–2424. doi: 10.1175/JPO2822.1

MacKinnon, J. A., & Gregg, M. C. (2005b). Spring mixing: Turbulence and internal waves during restratification on the New England shelf. *Journal of Physical Oceanography*, *35*(12), 2425–2443. doi: 10.1175/JPO2821.1

Merckelbach, L., Berger, A., Krahmann, G., Dengler, M., & Carpenter, J. R. (2019). A dynamic flight model for Slocum gliders and implications for turbulence microstructure measurements. *Journal of Atmospheric and Oceanic Technology*, *36*(2), 281–296. doi: 10.1175/JTECH-D-18-0168.1

Merckelbach, L., Smeed, D., & Griffiths, G. (2010). Vertical water velocities from underwater gliders. *Journal of Atmospheric and Oceanic Technology*, *27*(3), 547–563. doi: 10.1175/2009JTECHO710.1

Muller-Karger, F. E., Varela, R., Thunell, R., Luerssen, R., Hu, C., & Walsh, J. J. (2005). The importance of continental margins in the global carbon cycle. *Geophysical Research Letters*, *32*(1), 1–4. doi: 10.1029/2004GL021346

Naveira Garabato, A. C., Frajka-Williams, E. E., Spingys, C. P., Legg, S., Polzin, K. L., Forryan, A., ... Meredith, M. P. (2019). Rapid mixing and exchange of deep-ocean waters in an abyssal boundary current. *Proceedings of the National Academy of Sciences of the United States of America*, *116*(27), 13233–13238. doi: 10.1073/pnas.1904087116

Oakey, N. S. (1982). Determination of the Rate of Dissipation of Turbulent Energy from Simultaneous Temperature and Velocity Shear Microstructure Measurements. *Journal of Physical Oceanography*.

O'Callaghan, J., & Elliott, F. (2022). *Ocean microstructure glider observations in cook strait, new zealand* [Dataset]. doi: 10.17882/89143

Osborn, T. (1980). Estimates of the Local Rate of Vertical Diffusion from Dissipation Measurements.

Peeters, J. C. H., Los, F. J., Jansen, R., Haas, H. A., Peperzak, L., & de Vries, I. (1995). The oxygen dynamics of the oyster ground, north sea. impact of eutrophication and environmental conditions. *Ophelia*, *42*(1), 257-288. doi: 10.1080/00785326.1995.10431508

Peterson, A. K., & Fer, I. (2014). Dissipation measurements using temperature microstructure from an underwater glider. *Methods in Oceanography*. doi: 10.1016/j.mio.2014.05.002

Polzin, K. L., & McDougall, T. J. (2022). Chapter 7 - mixing at the ocean's bottom boundary. In M. Meredith & A. Naveira Garabato (Eds.), *Ocean mixing* (p. 145-180). Elsevier.

Rippeth, T. P., Fisher, N. R., & Simpson, J. H. (2001). The cycle of turbulent dissipation in the presence of tidal straining. *Journal of Physical Oceanography*, *31*(8 PART 2), 2458–2471. doi: 10.1175/1520-0485(2001)031⟨2458:tcotdi⟩2.0.co;2

Rippeth, T. P., Wiles, P., Palmer, M. R., Sharples, J., & Tweddle, J. (2009). The diapcynal nutrient flux and shear-induced diapcynal mixing in the seasonally stratified western Irish Sea. *Continental Shelf Research*, *29*(13), 1580–1587. doi: 10.1016/j.csr.2009.04.009

Salehipour, H., & Peltier, W. R. (2015). Diapycnal diffusivity, turbulent Prandtl number and mixing efficiency in Boussinesq stratified turbulence. *Journal of Fluid Mechanics*, *775*, 464–500. doi: 10.1017/jfm.2015.305

Salehipour, H., Peltier, W. R., Whalen, C. B., & MacKinnon, J. A. (2016). A new characterization of the turbulent diapycnal diffusivities of mass and momentum in the ocean. *Geophysical Research Letters*, *43*(7), 3370–3379. doi: 10.1002/2016GL068184

Sandstrom, H., & Elliott, J. A. (1984, July). Internal tide and solitons on the Scotian Shelf: A nutrient pump at work. *Journal of Geophysical Research*, *89*(C4), 6415-6426.

Scheifele, B., Waterman, S., Merckelbach, L., & Carpenter, J. (2018). Measuring the Dissipation Rate of Turbulent Kinetic Energy in Strongly Stratified, Low-Energy Environments: A Case Study From the Arctic Ocean. *Journal of Geophysical Research: Oceans*. doi: 10.1029/2017JC013731

Schultze, Merckelbach, L. M., & Carpenter, J. R. (2017). Turbulence and Mixing in a Shallow Shelf Sea From Underwater Gliders. *Journal of Geophysical Research: Oceans*, *122*(11), 9092–9109. doi: 10.1002/2017JC012872

Schultze, Merckelbach, L. M., & Carpenter, J. R. (2020). Storm-induced turbulence alters shelf sea vertical fluxes. *Limnology and Oceanography Letters*, *5*(3), 264–270. doi: 10.1002/lol2.10139

Sharples, J., Moore, C. M., & Abraham, E. R. (2001). Internal tide dissipation, mixing, and vertical nitrate flux at the shelf edge of NE New Zealand. *Journal of Geophysical Research: Oceans*, *106*, 69–81. doi: 10.1029/2000JC000604

Shih, L. H., Koseff, J. R., Ivey, G. N., & Ferziger, J. H. (2005). Parameterization of turbulent fluxes and scales using homogeneous sheared stably stratified turbulence simulations. *Journal of Fluid Mechanics*. doi: 10.1017/S0022112004002587

Simpson, J. H., Burchard, H., Fisher, N. R., & Rippeth, T. P. (2002). The semidiurnal cycle of dissipation in a ROFI. , *22*, 1615–1628.

Simpson, J. H., & Sharples, J. (2012). *Introduction to the physical and biological oceanography of shelf seas*. Cambridge University Press. doi: 10.1017/CBO9781139034098

Smyth, W. D., Moum, J. N., & Caldwell, D. R. (2002). The Efficiency of Mixing in Turbulent Patches: Inferences from Direct Simulations and Microstructure Observations. *Journal of Physical Oceanography*. doi:

10.1175/1520-0485(2001)031⟨1969:teomit⟩2.0.co;2

Smyth, W. D., Nash, J. D., & Moum, J. N. (2019). Self-organized criticality in geophysical turbulence. *Scientific Reports*, *9*(1), 1–8. doi: 10.1038/s41598-019-39869-w

St. Laurent, L., & Merrifield, S. (2017). Measurements of near-surface turbulence and mixing from autonomous ocean gliders. *Oceanography*, *30*(2), 116–125. doi: 10.5670/OCEANOG.2017.231

Stevens. (2014). Residual Flows in Cook Strait, a Large Tidally Dominated Strait. *Journal of Physical Oceanography*. doi: 10.1175/jpo-d-13-041.1

Stevens. (2018). Turbulent length scales in a fast-flowing, weakly stratified, strait: Cook Strait, New Zealand. *Ocean Science*, *14*(4), 801–812. doi: 10.5194/os-14-801-2018

Stevens, Smith, M. J., Grant, B., Stewart, C. L., & Divett, T. (2012). Tidal energy resource complexity in a large strait: The Karori Rip, Cook Strait. *Continental Shelf Research*, *33*, 100–109. doi: 10.1016/j.csr.2011.11.012

Tanaka, Y., Yasuda, I., Osafune, S., Tanaka, T., Nishioka, J., & Volkov, Y. N. (2014). Internal tides and turbulent mixing observed in the Bussol Strait. *Progress in Oceanography*, *126*, 98–108. doi: 10.1016/j.pocean.2014.04.009

Thomas, H., Bozec, Y., Elkalay, K., & De Baar, H. J. (2004). Enhanced Open Ocean Storage of CO2 from Shelf Sea Pumping. *Science*, *304*(5673), 1005–1008. doi: 10.1126/science.1095491

Umlauf, L., & Burchard, H. (2005). Second-order turbulence closure models for geophysical boundary layers. A review of recent work. *Continental Shelf Research*. doi: 10.1016/j.csr.2004.08.004

Umlauf, L., Burchard, H., & Bolding, K. (2012). GOTM-Sourcecode and Test Case Documentation. *Software Manual*, 346.

Valcarcel, A., Stevens, C., O'Callaghan, J., Suanda, S., & Grant, B. (2022). *Wind and current speeds in cook strait, new zealand* [Dataset]. doi: 10.17882/89142

Vennell, R. (1998a). Observations of the phase of tidal currents along a strait. *Journal of Physical Oceanography*, *28*(8), 1570–1577. doi: 10.1175/1520-0485(1998)028⟨1570:OOTPOT⟩2.0.CO;2

Vennell, R. (1998b). Oscillating barotropic currents along short channels. *Journal of Physical Oceanography*, *28*(8), 1561–1569. doi: 10.1175/1520-0485(1998)028⟨1561:OBCASC⟩2.0.CO;2

Vennell, R., & Collins, N. (1991). *Acoustic Doppler Current Profiler Measurements of Tides in Cook Strait, New Zealand.* "Coastal Engineering - Climate for Change" 10th Australasian Conference on Coastal and Ocean Engineering, Auckland, 2-6 Dec. 1991.

Verspecht, F., Rippeth, T. P., Howarth, M. J., Souza, A. J., Simpson, J. H., & Burchard, H. (2009). Processes impacting on stratification in a region of freshwater influence: Application to Liverpool Bay. *Journal of Geophysical Research: Oceans*, *114*(11), 1–12. doi: 10.1029/2009JC005475

Waskom, M. L. (2021). seaborn: statistical data visualization. *Journal of Open Source Software*, *6*(60), 3021.

Watanabe, M., & Hibiya, T. (2002). Global estimates of the wind-induced energy flux to inertial motions in the surface mixed layer. *Geophysical Research Letters*, *29*(8), 2–5. doi: 10.1029/2001GL014422

Waterhouse, A. F., Mackinnon, J. A., Nash, J. D., Alford, M. H., Kunze, E., Simmons, H. L., ... Lee, C. M. (2014). Global patterns of diapycnal mixing from measurements of the turbulent dissipation rate. *Journal of Physical Oceanography*, *44*(7), 1854–1872. doi: 10.1175/JPO-D-13-0104.1

Wesson, J. C., & Gregg, M. C. (1994). Mixing at Camarinal Sill in the Strait of Gibraltar. *Journal of Geophysical Research*, *99*(C5), 9847–9878. doi: 10.1029/94JC00256

Williams, C., Sharples, J., Mahaffey, C., & Rippeth, T. (2013). Wind-driven nutrient pulses to the subsurface chlorophyll maximum in seasonally stratified shelf seas. *Geophysical Research Letters*, *40*(20), 5467–5472. doi: 10.1002/2013GL058171

Winters, K. B., Lombard, P. N., Riley, J. J., & D'Asaro, E. A. (1995). Available potential energy and mixing in density-stratified fluids. *Journal of Fluid Mechanics*, *289*, 115–128. doi: 10.1017/S002211209500125X

Wolk, F., Lueck, R. G., & Laurent, L. S. (2009). Turbulence Measurements from a Glider Turbulence Package and Glider. *13th Workshop on Physical Processes in Natural Waters, Palermo*(September), 1–4.

Zeldis, J. R., Hadfield, M. G., & Booker, D. J. (2013). Influence of climate on pelorus sound mussel aquaculture yields: Predictive models and underlying mechanisms. *Aquaculture Environment Interactions*, *4*(1), 1–15. doi: 10.3354/aei00066

Zulberti, A., Jones, N. L., & Ivey, G. N. (2020). Observations of Enhanced Sediment Transport by Nonlinear Internal Waves. *Geophysical Research Letters*, *47*(19), 1–11. doi: 10.1029/2020GL088499

Zwillinger, D., & Kokoska, S. (2000). CRC Standard Probability and Statistics Tables and Formulae, Student Edition. *Journal of Open Source Software*.

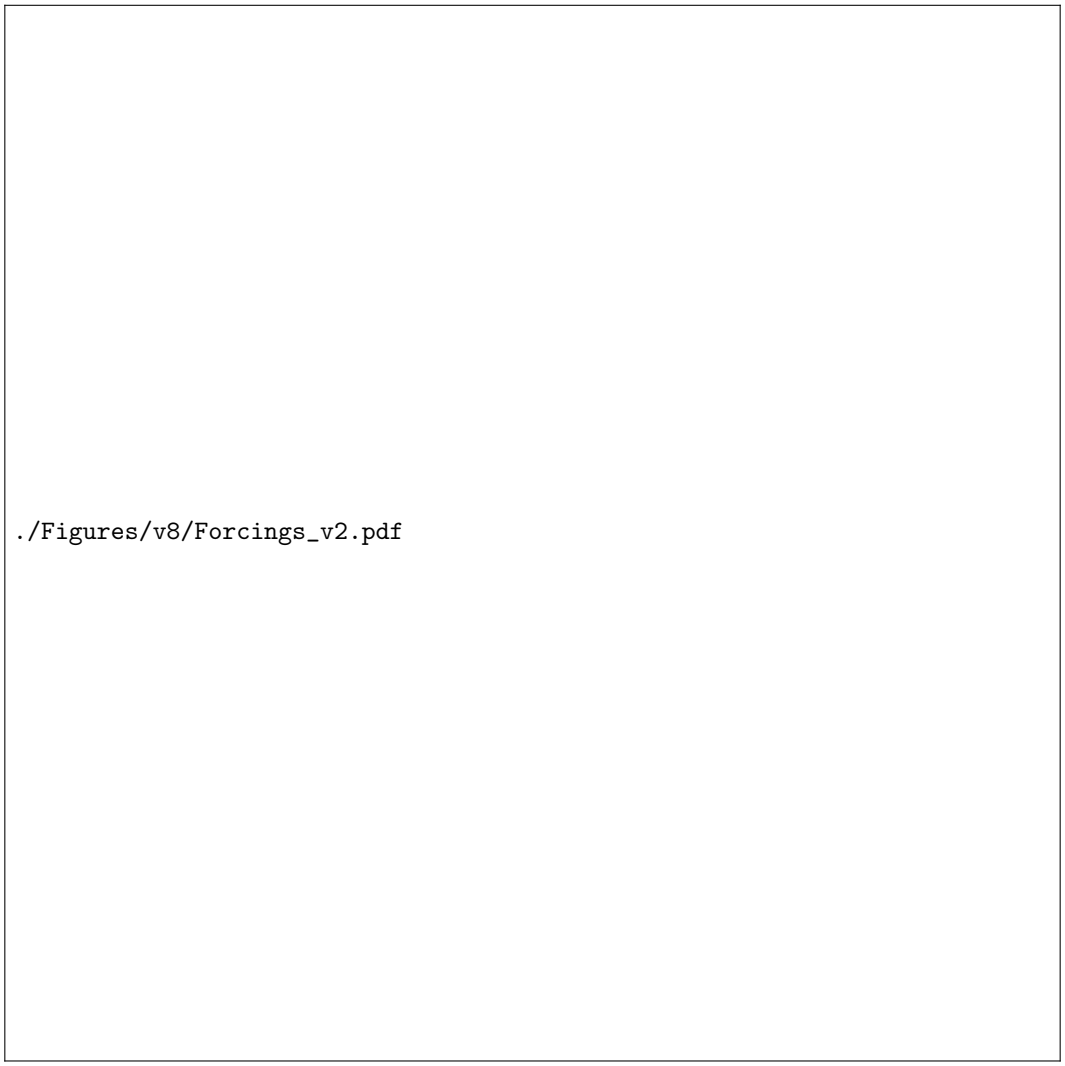

Figure 2. Large scale forcing of turbulent mixing at the study site, a combination of fast tidal flows and a strong wind perturbation. The figure shows depth-time series of (a) along and (b) cross-strait flow speeds (along the semi-major and semi-minor axes of the tidal ellipse respectively); time series of (c) sea height (brown axis and line) and along-strait tidal phase (red and blue mark maxima and minima in bottom shear respectively); time series of (d) Cape Campbell AWS wind speed at 10 m below (green) and above (orange) the 10.8 $\mathrm{m\,s^{-1}}$ threshold (dashed line).

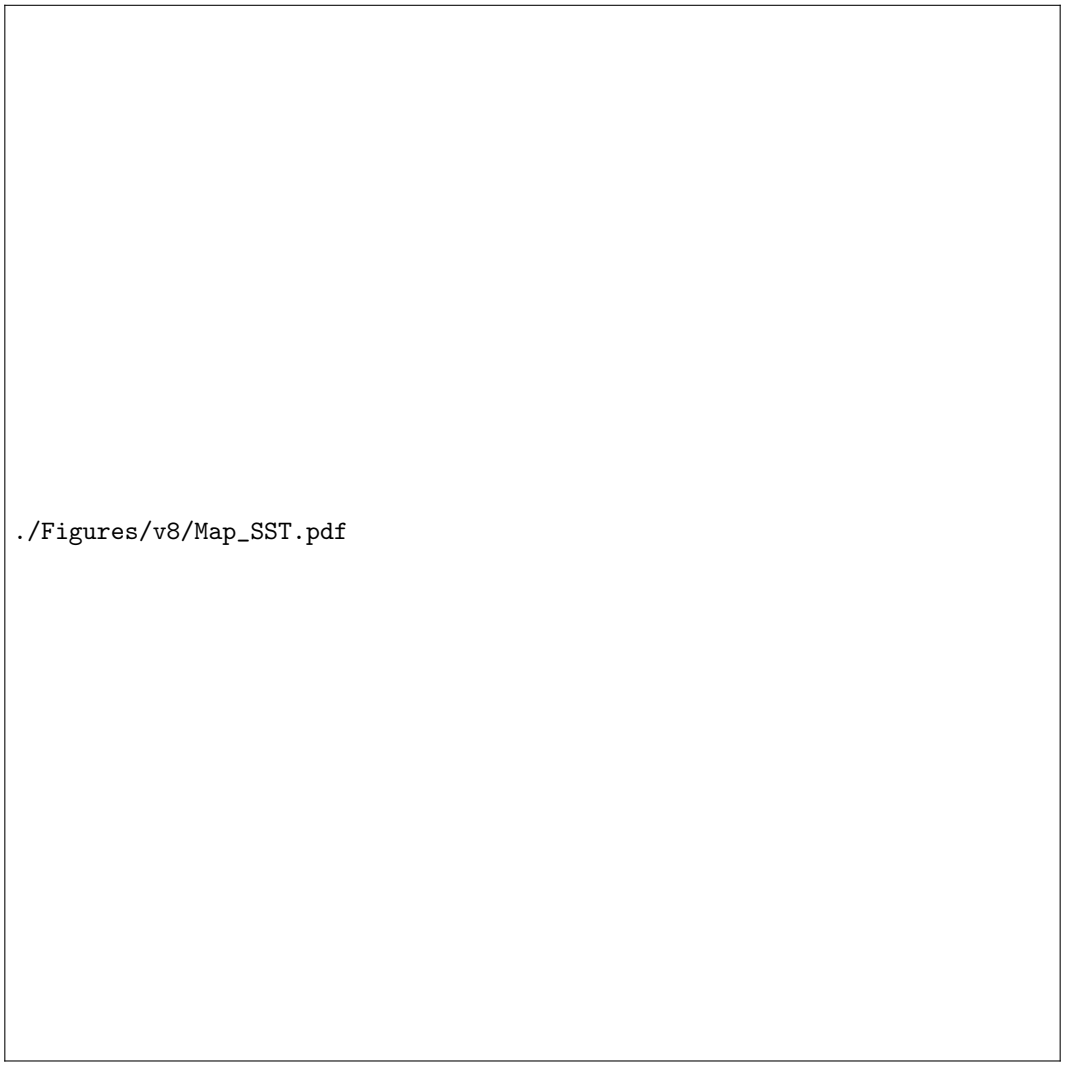

Figure 3. Overlay of OMG tracks and satellite-based SST measurements shows the connection between the observed "low density surface waters" and a larger scale surface temperature front. Maps of Te Moana o Raukawa - Cook Strait with satellite SST fields (horizontal colorbar), ADCP site (blue square marker) and OMG surfacings per time of day (circular markers, vertical colorbar) for the days (a) 23^{rd}, (b) 24^{th}, (b) 25^{th}, (b) 26^{th}, (b) 27^{th} of June.

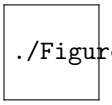

Figure 4. Variability of turbulence-driven mixing in a temperature-layered water column. Panel (a) shows the profile averaging bins for the low density surface waters (LDSW) events (purple and yellow top line), wind speed (green and orange middle line), tidal shear (red and blue bottom sinusoid). Panels (b)-(g) show the depth time series of Ocean Microstructure Glider observations of (b) potential temperature θ; (c) buoyancy frequency squared N^2; (d) dissipation rates ϵ; (e) turbulence intensity Re_b; (f) diapycnal diffusivity K_z; (g) dynamical stability Ri_g^{-1}. For the (b)-(g) panels, the black (red) lines indicate the top (bottom) edge of the mid-layer and the thick black dashed line indicates the seabed. For all panels the black rectangles mark full water column homogeneity.

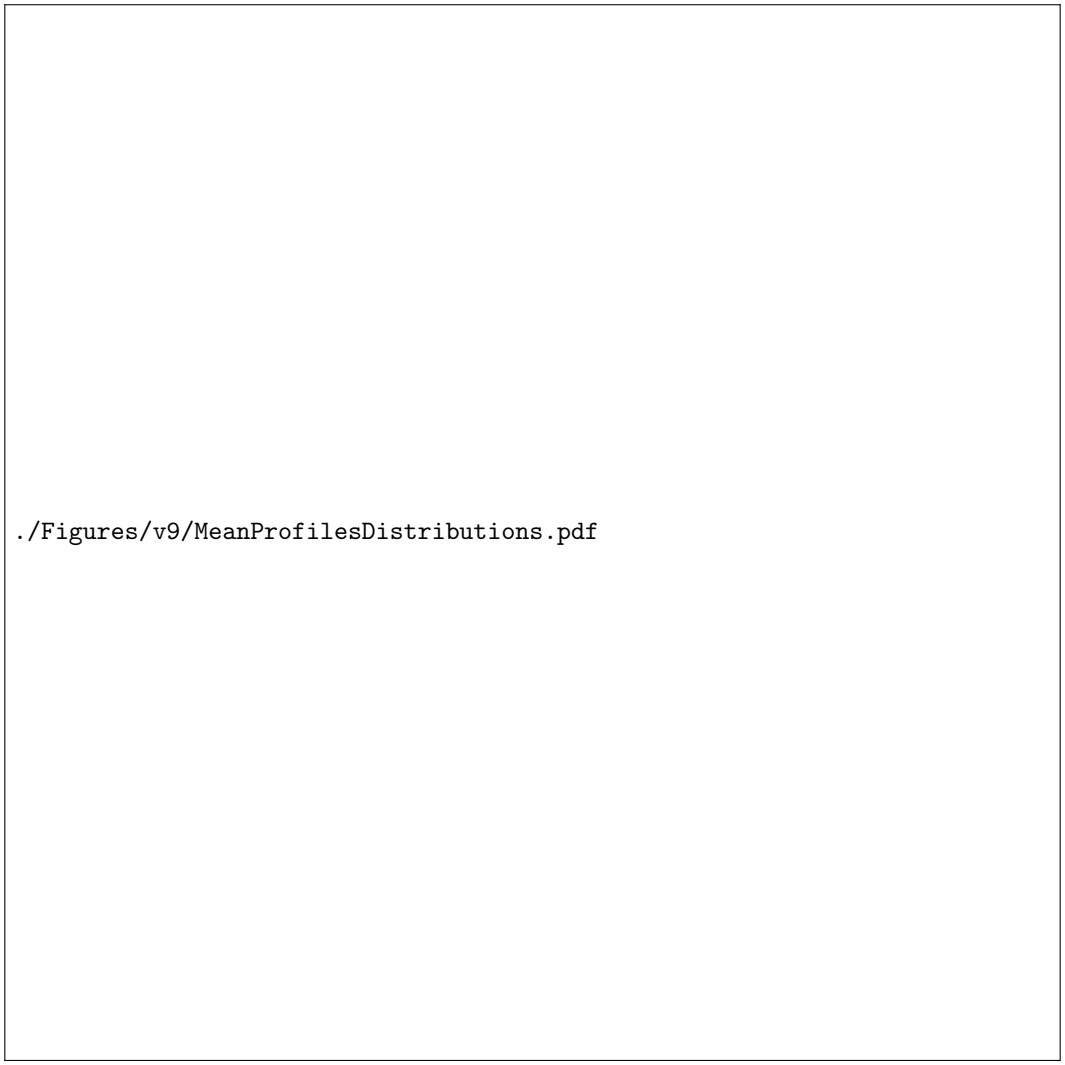

Figure 5. Intense mixing from elevated dissipation and weak stratification in boundary mixing-layers and relatively less active mixing from stronger stratification and lower dissipation rates in the mid-layer. Log-averaged profiles along normalized water column ($\hat{z}$, top row) and probability density function (PDF, bottom row) of (a)-(b) dissipation rates ϵ, (c)-(d) buoyancy frequency squared N^2 and (e)-(f) turbulence intensity Re_b. For all panels, blue indicates the surface mixing-layer, orange the mid-layer and green the bottom mixing-layer. In the top row, the dark lines indicate the mean values and the lighter envelope show the ± 1 standard deviation intervals. In the bottom row, the solid lines indicate the curve fit of the underlying lighter coloured histograms, and the dashed lines mark the mean value of each distribution.

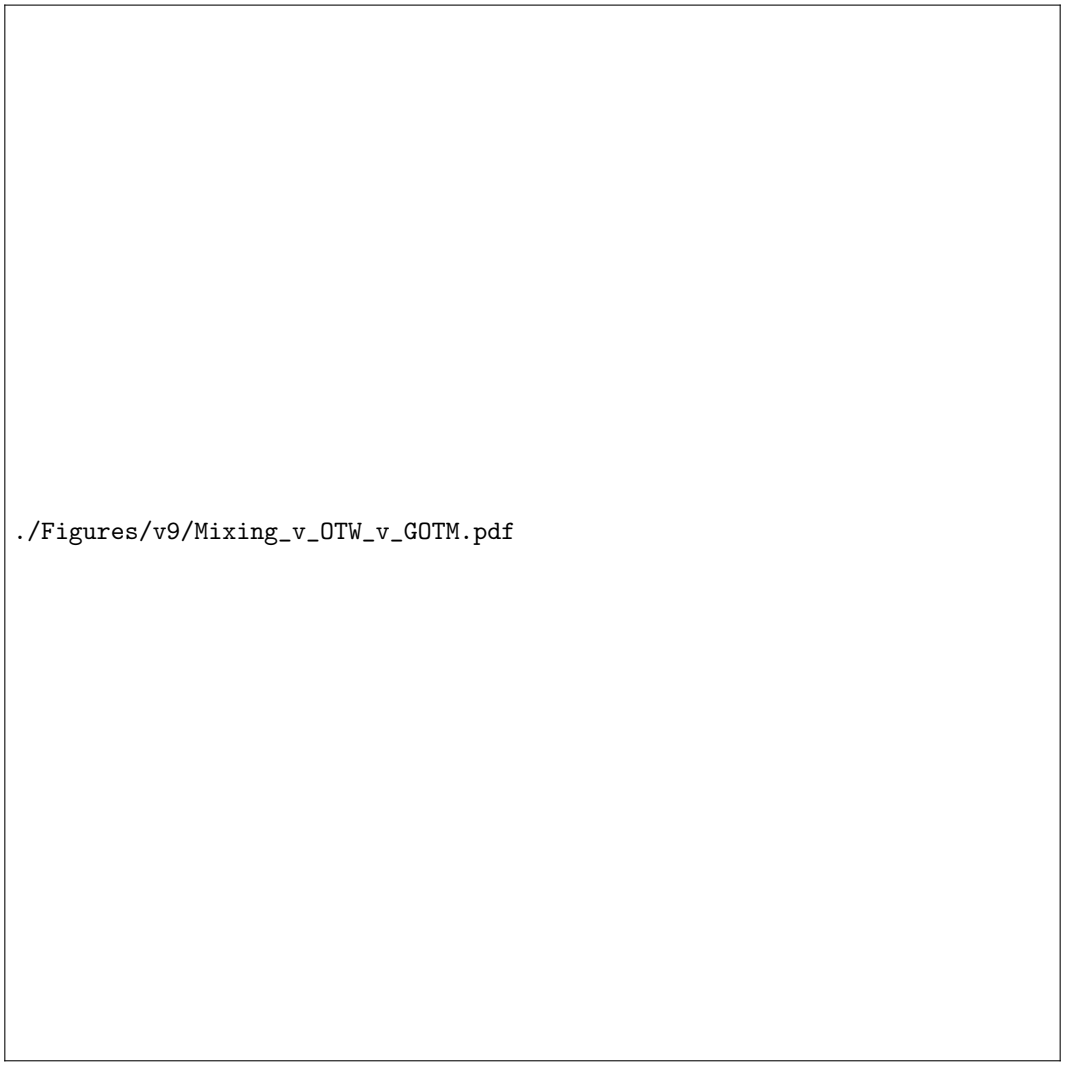

Figure 6. One-dimensional models of dissipation rate qualitatively match some aspects of the variability in the observations and compare well quantitatively to some portions of the observations. Depth-time series of dissipation rates ϵ as (a) microstructure (OMG) observations; (b) law of-the-wall (LoW) estimates; (c) turbulence model (GOTM) estimates.

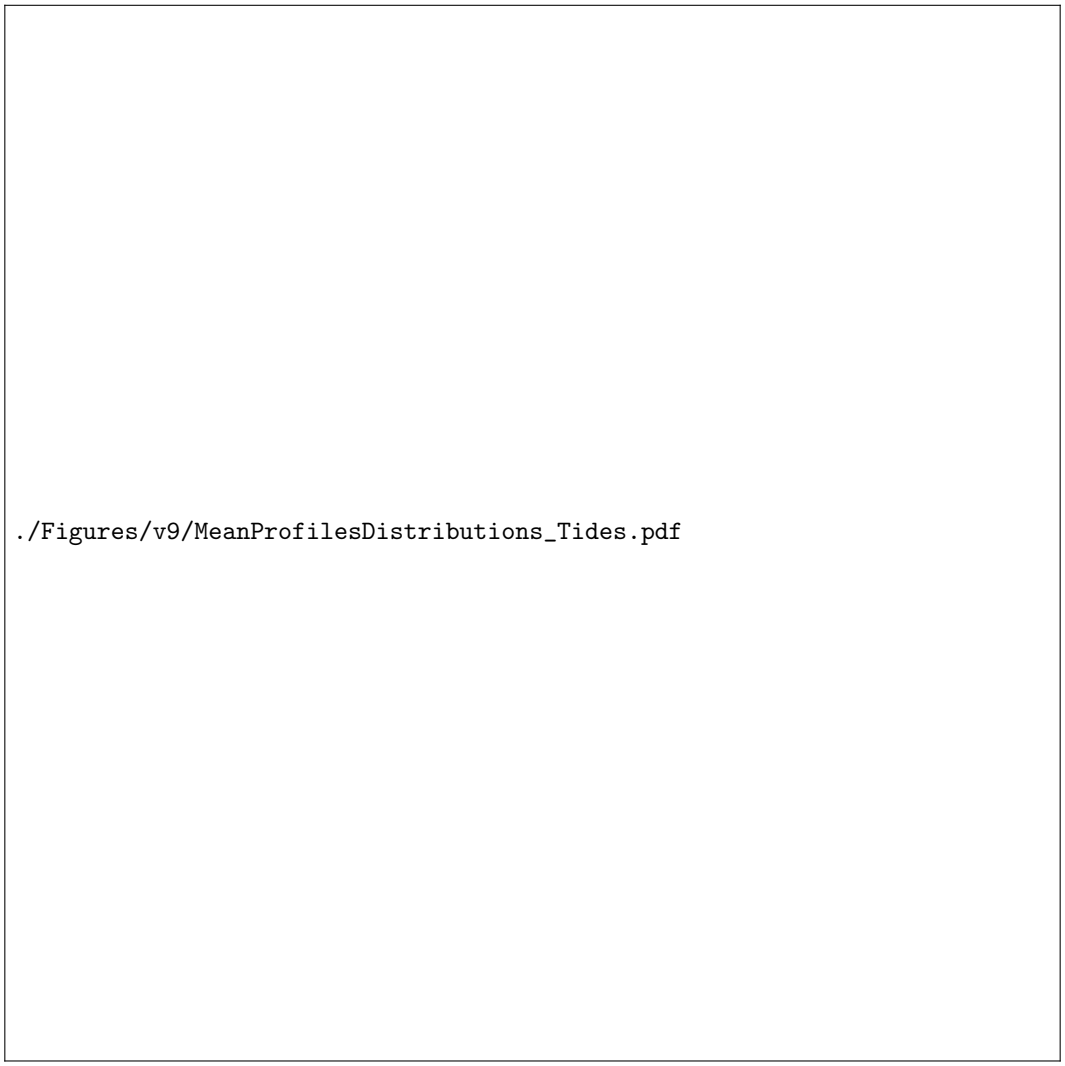

Figure 7. Two regimes of shear-driven dissipation rates in the bottom mixing-layer, compared to GOTM estimates of dissipation and shear production. (a) log-averaged profiles along normalized depth ($\hat{z}$) of dissipation rates ϵ from the observations (light-colored continuous lines, with ± 1 standard deviation interval shaded), and GOTM estimates (dark-colored dashed lines). (b) log-averaged profiles along normalized depth ($\hat{z}$) of GOTM estimates of shear production rates P (dark-colored dashed lines, with ± 1 standard deviation interval shaded). Probability density function (PDF) of observed ϵ (c) and GOTM estimates of P (d) in the bottom mixing-layer.

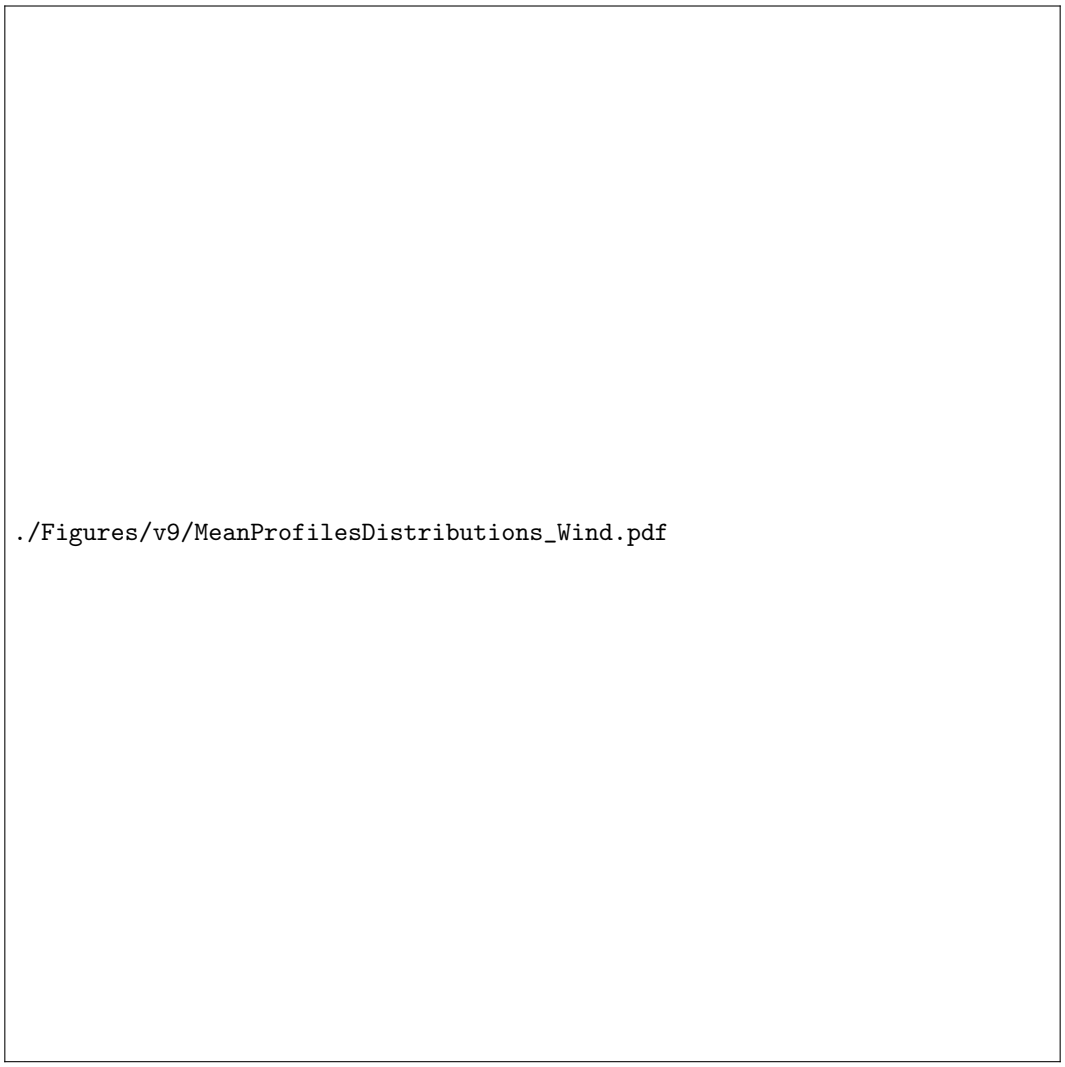

Figure 8. Two regimes of wind-driven dissipation rates in the surface mixing-layer, compared to GOTM estimates of dissipation and shear production. (a) log-averaged profiles along normalized depth ($\hat{z}$) of dissipation rates ϵ from the observations (light-colored continuous lines, with ± 1 standard deviation interval shaded), and GOTM estimates (dark-colored dashed lines). (b) log-averaged profiles along normalized depth ($\hat{z}$) of GOTM estimates of shear production rates P (dark-colored dashed lines, with ± 1 standard deviation interval shaded). Probability density function (PDF) of observed ϵ (c) and GOTM estimates of P (d) in the surface mixing-layer.

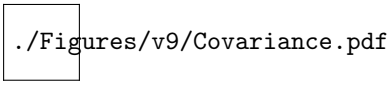

Figure 9. Strength of the relationship as rank correlation coefficients between ϵ and color-coded variables along the normalized water depth $\hat{z}$. Dark grey shaded area indicates weak correlation, light grey indicates the seabed. Black and red dashed lines indicate the average top and bottom edge of the mid-layer, respectively.

Figure 10. Total production estimates from GOTM compare well to observed dissipation rates, especially near the boundaries of the normalized water column. The figure shows color-coded scatter of normalized depth ($\hat{z}$) averaged values between estimates of total production from GOTM (P+G) and observed dissipation ϵ (circular markers with standard deviation error bars) or ϵ estimates from GOTM (cross markers). Black bars indicate the average values of shear production P alone.

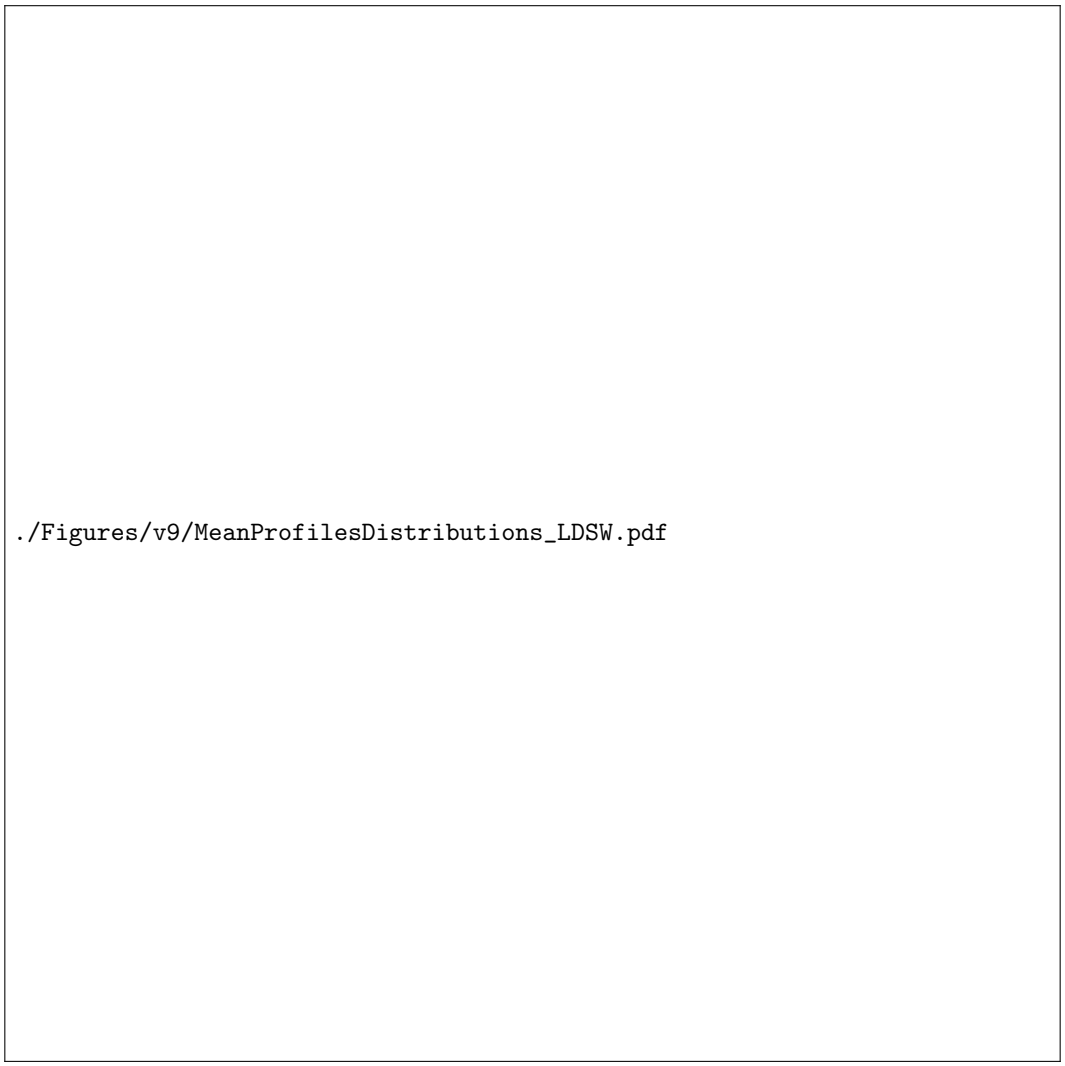

Figure 11. Low density surface waters in the dataset linked to a surface front of high SST advected through the narrows, isolates bottom and surface mixing-layers by significantly reducing the vertical diffusivity of mass. Panel (a) shows average profiles with normalized depth ($\hat{z}$) of the canonical vertical diffusivity of mass (K_z) during a low density surface waters event or not (yellow or purple respectively) as indicated in panel (a) of Figure 4. In panel (a), the dark lines indicate the mean values and the lighter envelope show the 95% confidence intervals. Panel (b) show the PDF of diapycnal diffusivity according to each bin, where the solid lines indicate the curve fit of the underlying lighter coloured histograms, and the dashed lines mark the mean value of each distribution.

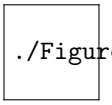

Figure 12. Presence of low density surface waters stabilizes the mean flow and reduces turbulence intensity. Scatter plot and marginal distribution envelopes of turbulence intensity (Re_b) against dynamical stability (Ri_g^{-1}). Regression lines for the full dataset (black, dashed), in (yellow, continuous) and out (purple, continuous) of LDSW are indicated. Horizontal and vertical dashed lines indicate the critical value for dynamical stability $Ri_g^{-1} = 4$ and the transitional value towards isotropic turbulence $Re_b = 1 \times 10^2$, respectively.

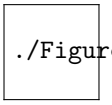

Figure 13. Elevated observed dissipation rates linked to the state of criticality of both the observed mean flow dynamical stability (Ri_g^{-1}) and the modelled mixing efficiency (R_f^{-1}). Scatter plot and marginal distribution envelopes of dynamical stability (Ri_g^{-1}) as a function of mixing efficiency (R_f^{-1}), for 3 color-coded equi-partitioned intervals of the distribution of dissipation rates ϵ (ϵ_{low}, ϵ_{mid} and ϵ_{high} in the $[0; 33^{rd}]$,$]33^{rd}; 66^{th}]$ and $]66^{th}; 100^{th}]$ percentile intervals; with transition values $\epsilon_{33^{rd}}$ and $\epsilon_{66^{th}}$ of 1.7×10^{-8} and $6.5 \times 10^{-8}\,\mathrm{W\,kg^{-1}}$), with Ri_g^{-1}-R_f^{-1} log-averages and ± 1 standard deviations indicated by marker and error bar respectively. Regression lines for all ϵ values (dashed, black), each ϵ interval (continuous, color-coded), and median values (continuous, black) are indicated. Vertical and horizontal dashed lines indicate the critical values for dynamical instability ($Ri_g^{-1} > 4$) and turbulence growth ($R_f^{-1} > 0.17^{-1}$), respectively.

Figure 1.

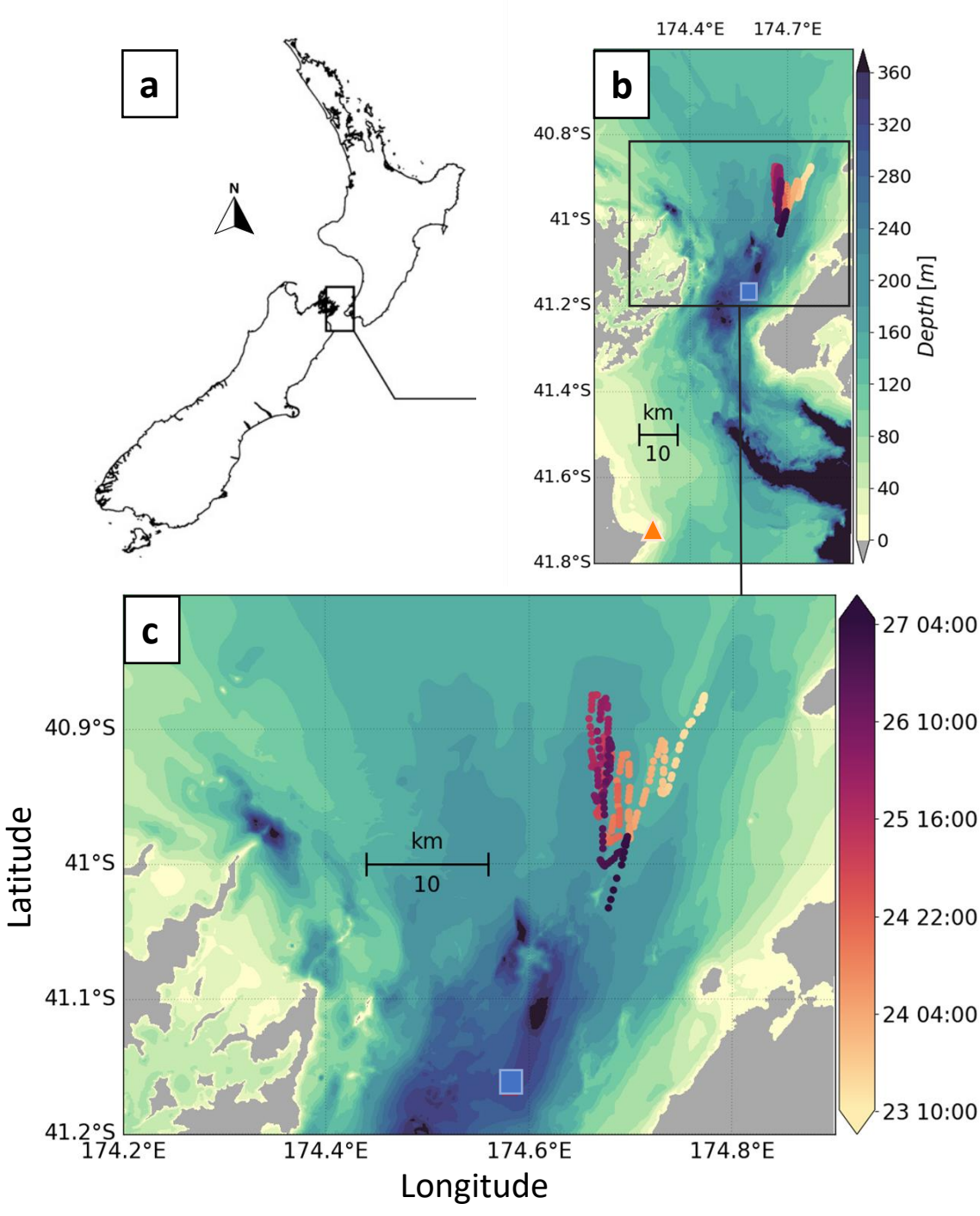
a
N
b
174.4°E
174.7°E
40.8°S
41°S
41.2°S
41.4°S
41.6°S
41.8°S
km
10
360
320
280
240
200
160
120
80
40
0
Depth [m]
c
40.9°S
41°S
41.1°S
41.2°S
174.2°E
174.4°E
174.6°E
174.8°E
Latitude
Longitude
27 04:00
26 10:00
25 16:00
24 22:00
24 04:00
23 10:00

Figure 2.

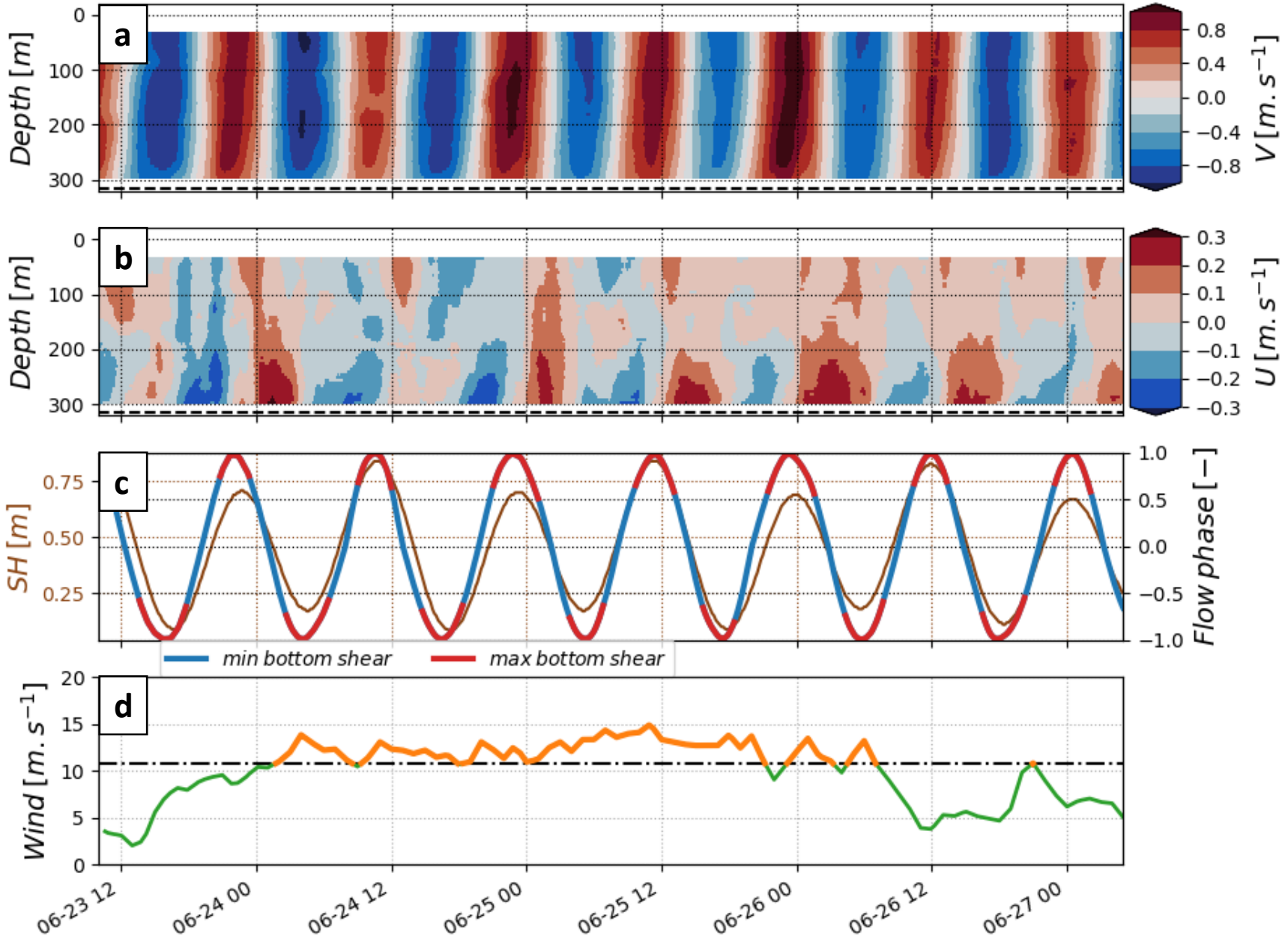
a
Depth [m]
0
100
200
300
0.8
0.4
0.0
−0.4
−0.8
V [m. s−1]
b
Depth [m]
0
100
200
300
0.3
0.2
0.1
0.0
−0.1
−0.2
−0.3
U [m. s−1]
c
SH [m]
0.75
0.50
0.25
1.0
0.5
0.0
−0.5
−1.0
Flow phase [−]
min bottom shear
max bottom shear
d
Wind [m. s−1]
20
15
10
5
0
06-23 12
06-24 00
06-24 12
06-25 00
06-25 12
06-26 00
06-26 12
06-27 00

Figure 3.

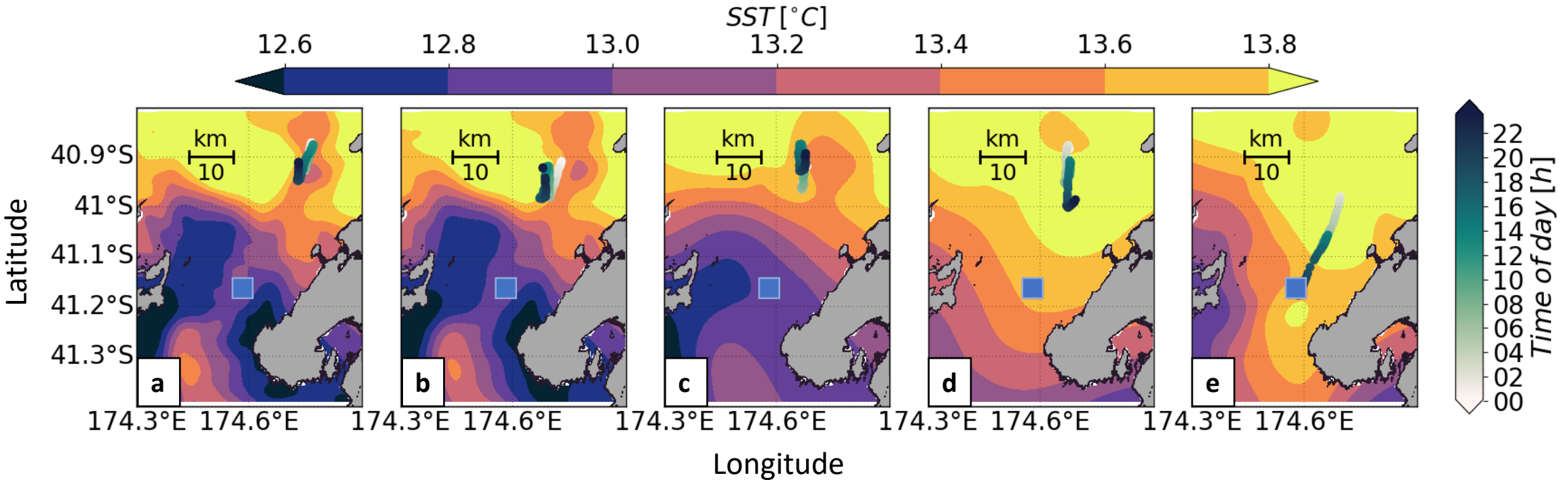
SST [°C]
12.6
12.8
13.0
13.2
13.4
13.6
13.8
Latitude
40.9°S
41°S
41.1°S
41.2°S
41.3°S
km
10
a
b
c
d
e
174.3°E
174.6°E
Longitude
Time of day [h]
22
20
18
16
14
12
10
08
06
04
02
00

Figure 4.

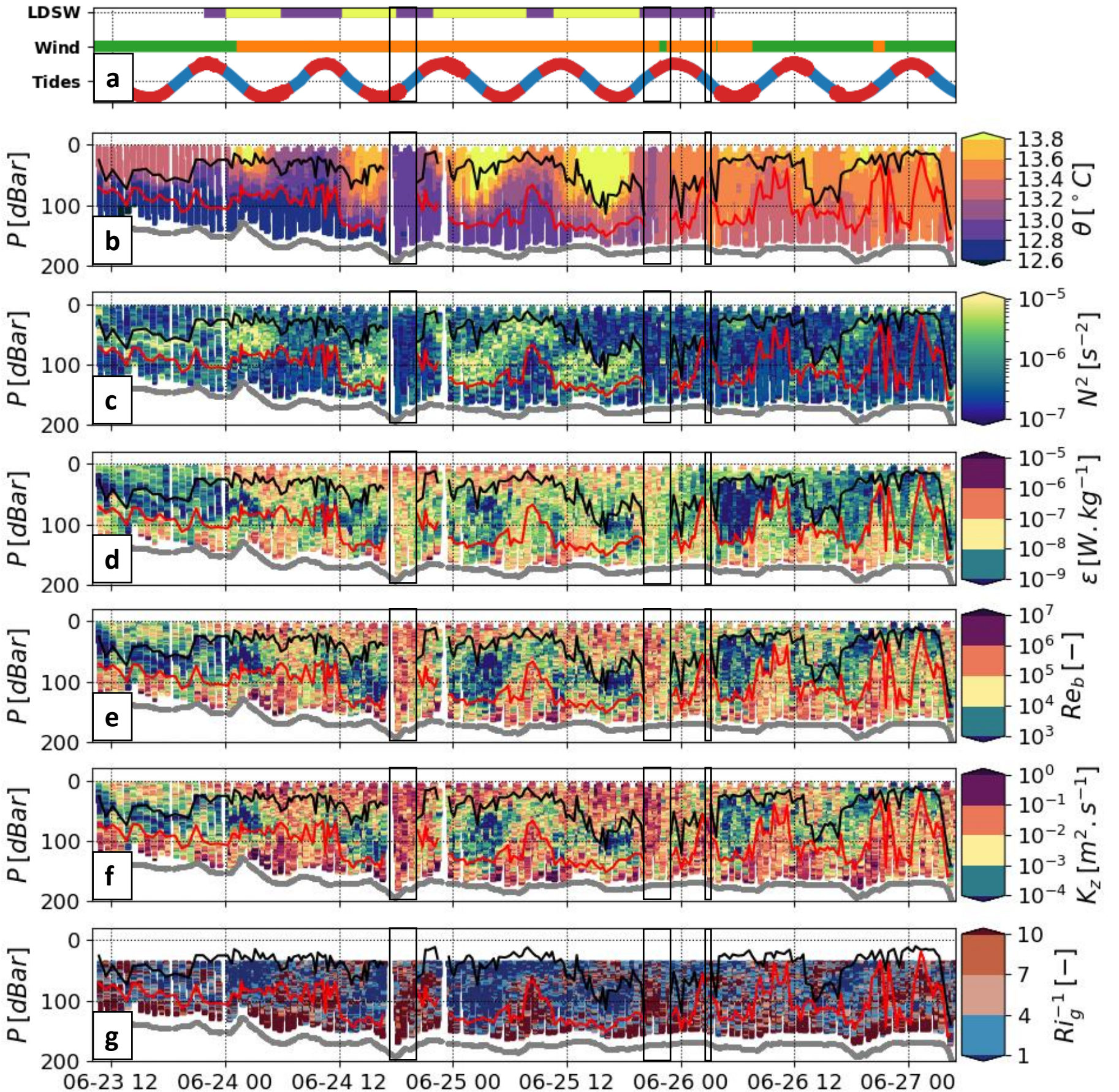
LDSW
Wind
Tides
a
b
c
d
e
f
g
P [dBar]
0
100
200
θ [°C]
13.8
13.6
13.4
13.2
13.0
12.8
12.6
N² [s⁻²]
10⁻⁵
10⁻⁶
10⁻⁷
ε [W.kg⁻¹]
10⁻⁵
10⁻⁶
10⁻⁷
10⁻⁸
10⁻⁹
Re_b [−]
10⁷
10⁶
10⁵
10⁴
10³
K_z [m².s⁻¹]
10⁰
10⁻¹
10⁻²
10⁻³
10⁻⁴
Ri_g⁻¹ [−]
10
7
4
1
06-23 12
06-24 00
06-24 12
06-25 00
06-25 12
06-26 00
06-26 12
06-27 00

Figure 5.

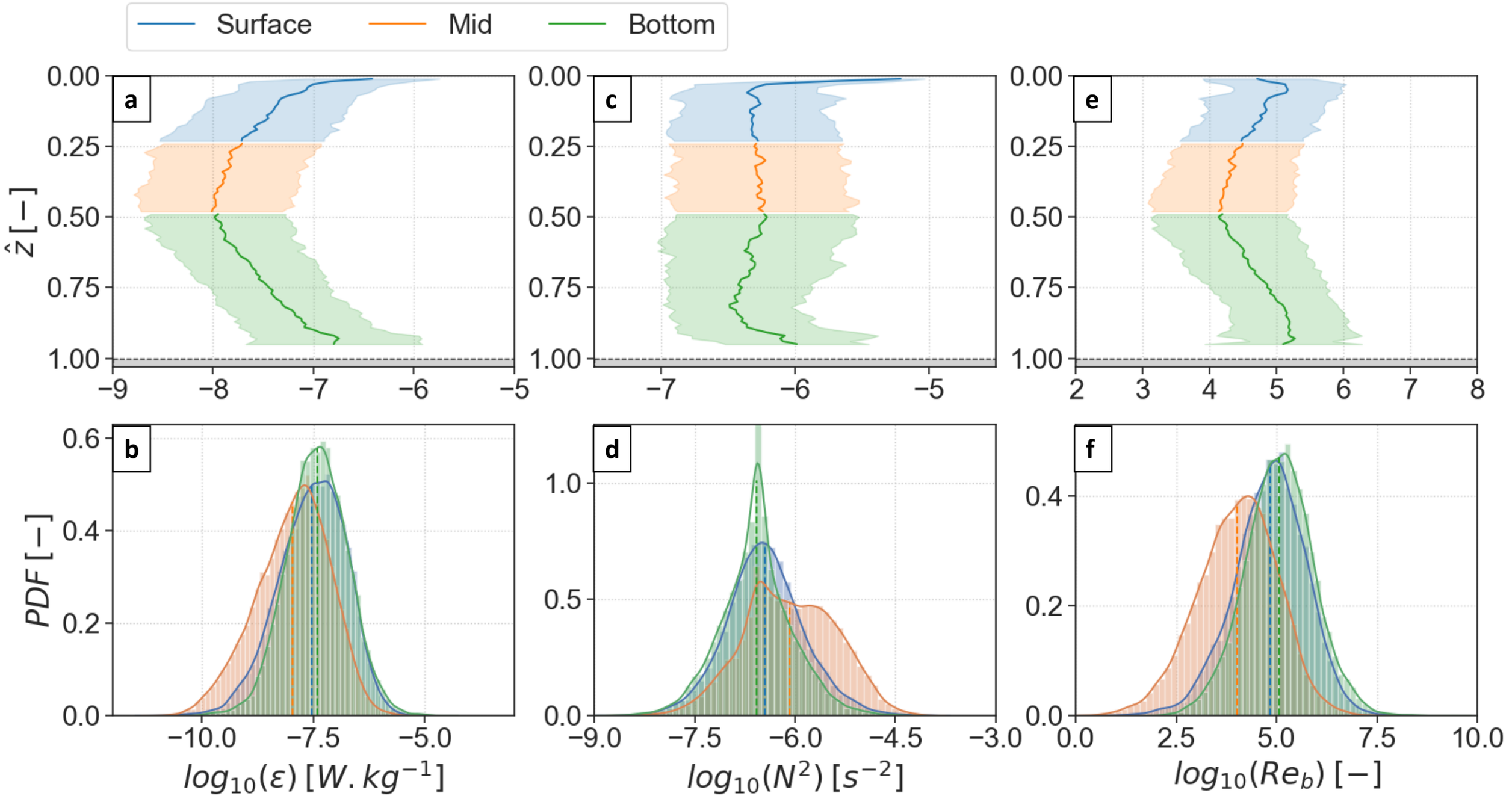
Surface
Mid
Bottom
a
b
c
d
e
f
$\hat{z}$ [−]
PDF [−]
$log_{10}(\varepsilon)\,[W.kg^{-1}]$
$log_{10}(N^2)\,[s^{-2}]$
$log_{10}(Re_b)$ [−]

Figure 6.

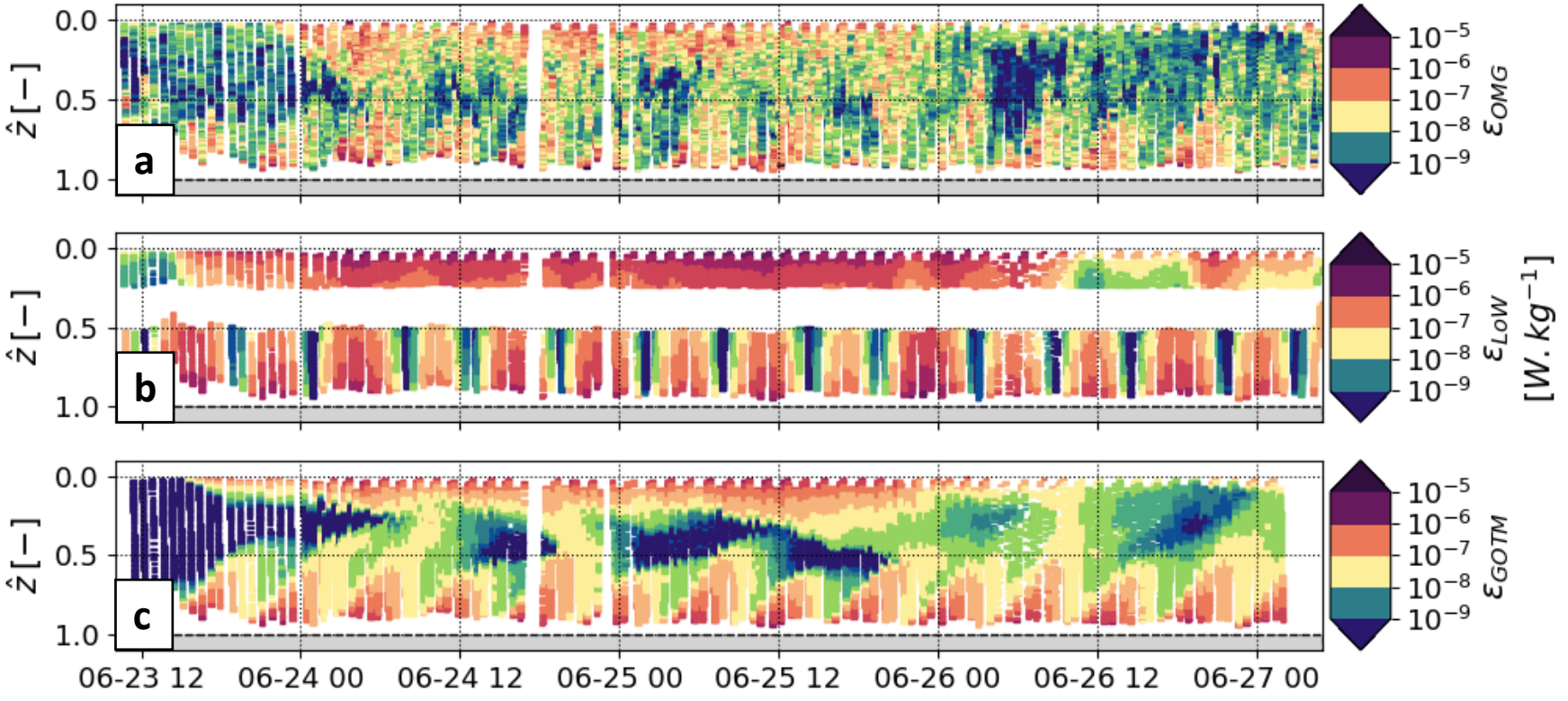
0.0
0.5
1.0
$\hat{z}$ [−]
a
b
c
10^{-5}
10^{-6}
10^{-7}
10^{-8}
10^{-9}
ε_{OMG}
ε_{LoW}
ε_{GOTM}
$[W.kg^{-1}]$
06-23 12
06-24 00
06-24 12
06-25 00
06-25 12
06-26 00
06-26 12
06-27 00

Figure 7.

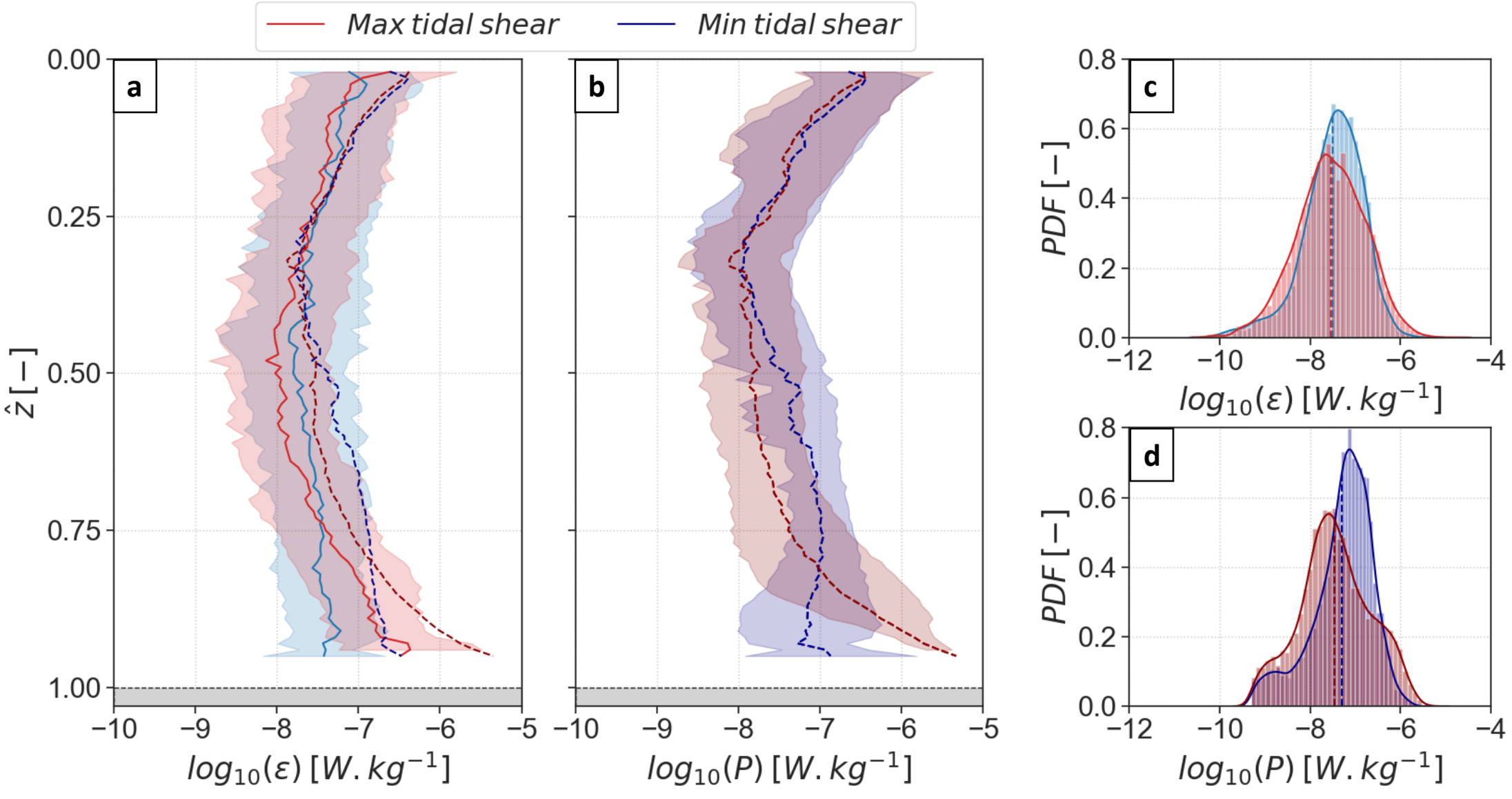
Max tidal shear
Min tidal shear
a
b
c
d
$\hat{z}$ [−]
0.00
0.25
0.50
0.75
1.00
−10
−9
−8
−7
−6
−5
$log_{10}(\varepsilon)\ [W.kg^{-1}]$
$log_{10}(P)\ [W.kg^{-1}]$
PDF [−]
0.0
0.2
0.4
0.6
0.8
−12
−10
−8
−6
−4

Figure 8.

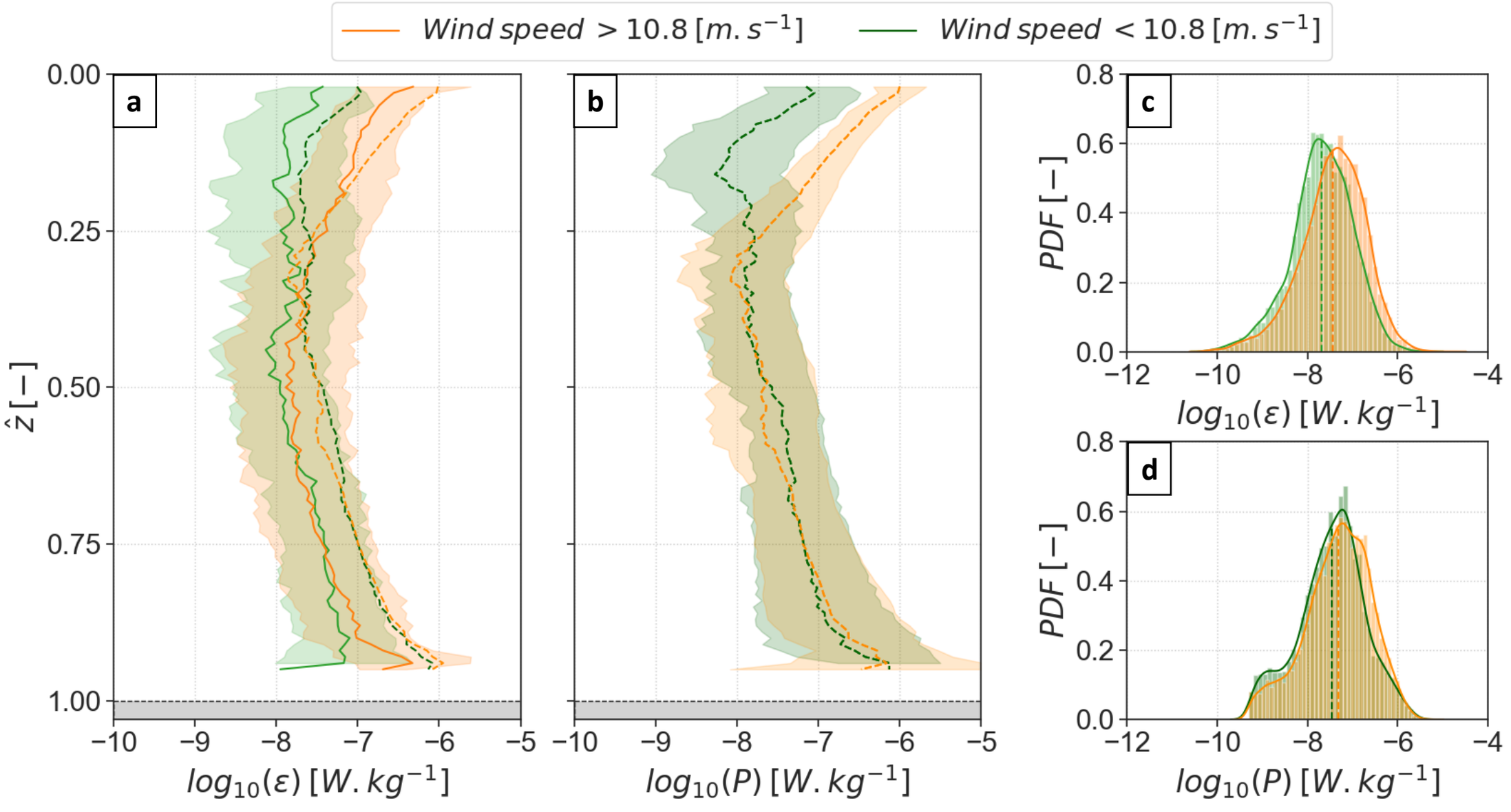
Wind speed > 10.8 [m. s⁻¹]
Wind speed < 10.8 [m. s⁻¹]
a
b
c
d
ẑ [−]
0.00
0.25
0.50
0.75
1.00
−10
−9
−8
−7
−6
−5
log₁₀(ε) [W. kg⁻¹]
log₁₀(P) [W. kg⁻¹]
PDF [−]
0.0
0.2
0.4
0.6
0.8
−12
−10
−8
−6
−4

Figure 9.

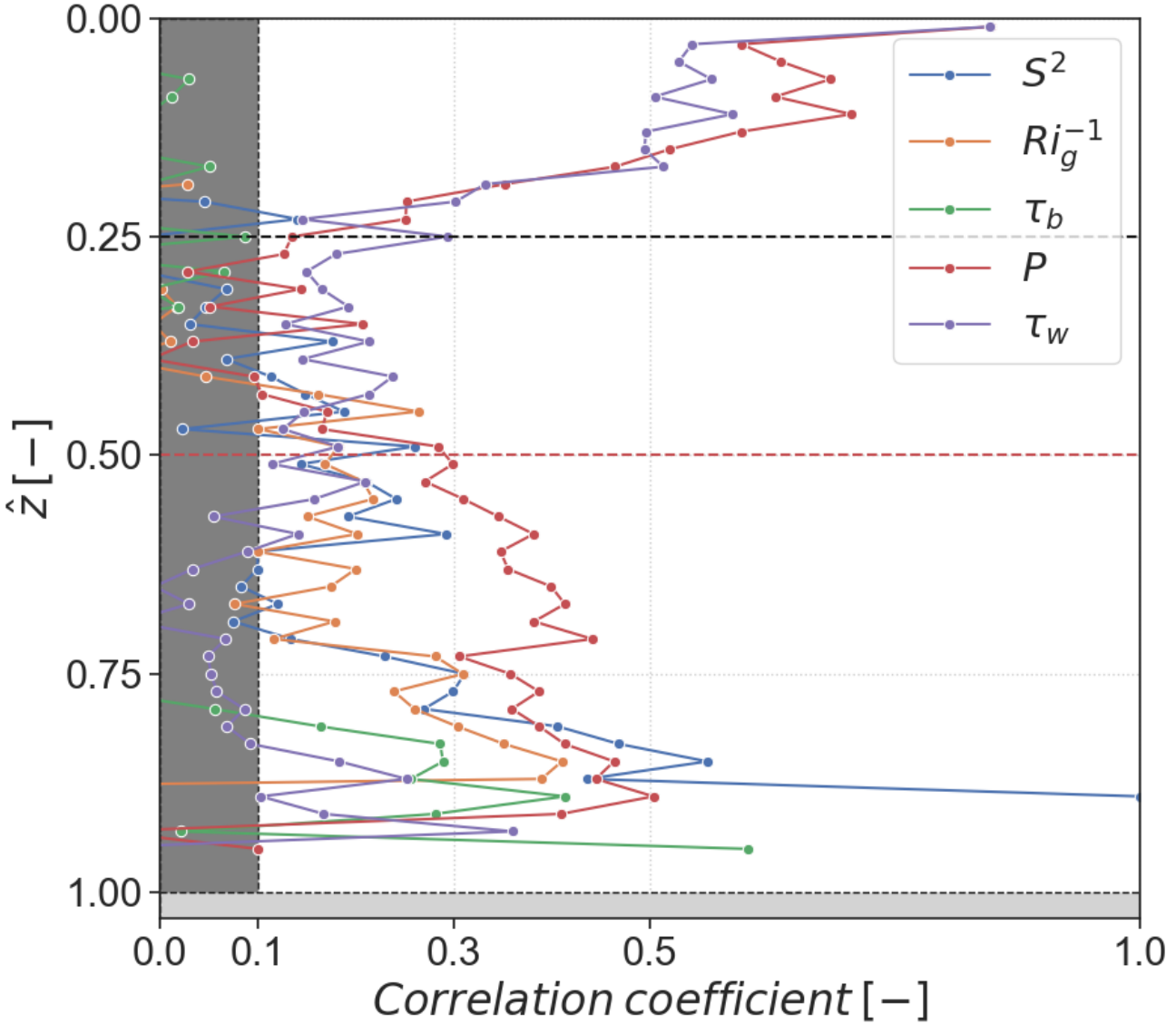
0.00
0.25
0.50
0.75
1.00
$\hat{z}$ [−]
0.0
0.1
0.3
0.5
1.0
Correlation coefficient [−]
S^2
Ri_g^{-1}
τ_b
P
τ_w

Figure 10.

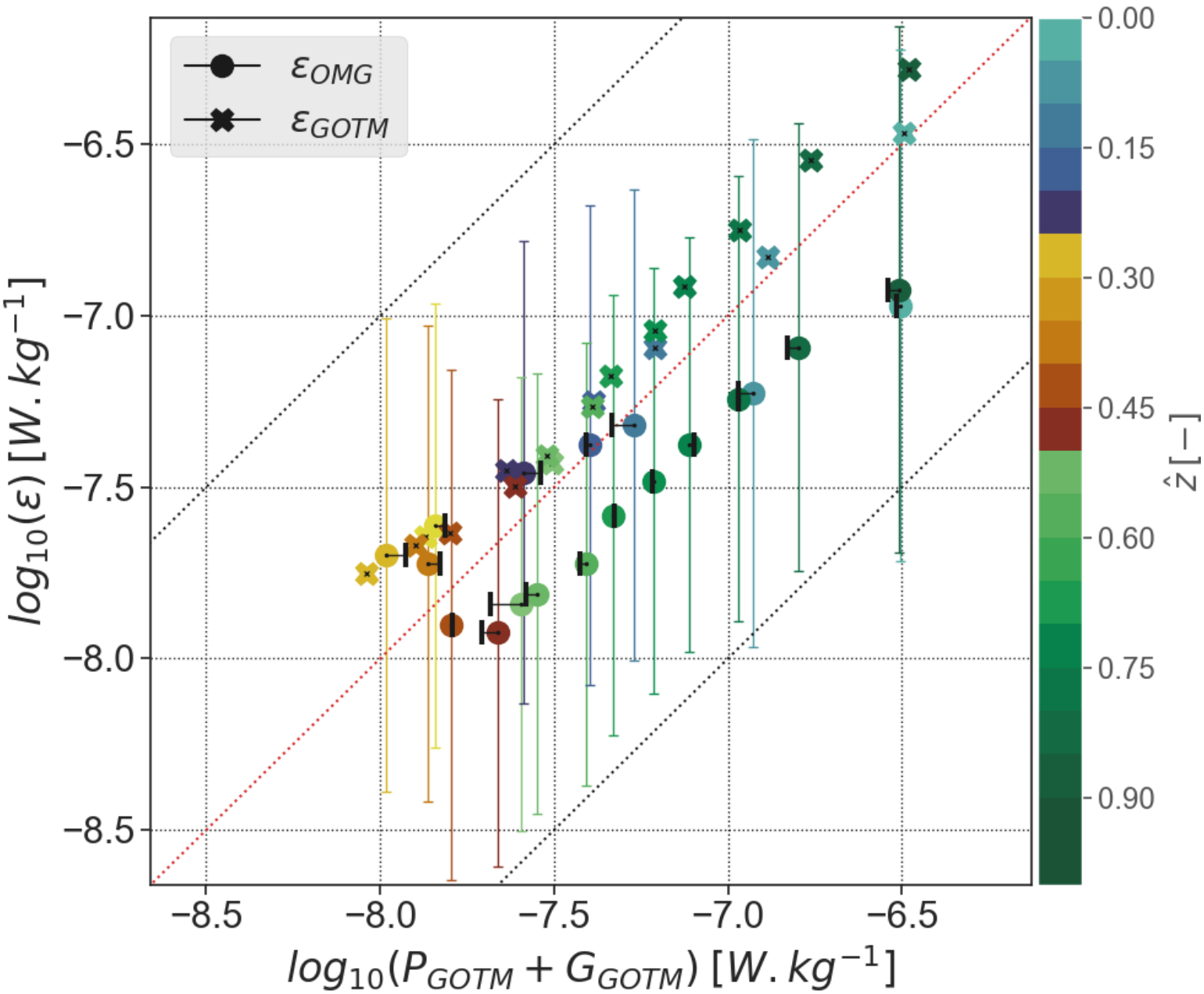
ε_{OMG}
ε_{GOTM}
$log_{10}(\varepsilon)\,[W.kg^{-1}]$
$log_{10}(P_{GOTM} + G_{GOTM})\,[W.kg^{-1}]$
−6.5
−7.0
−7.5
−8.0
−8.5
$\hat{z}$ [−]
0.00
0.15
0.30
0.45
0.60
0.75
0.90

Figure 11.

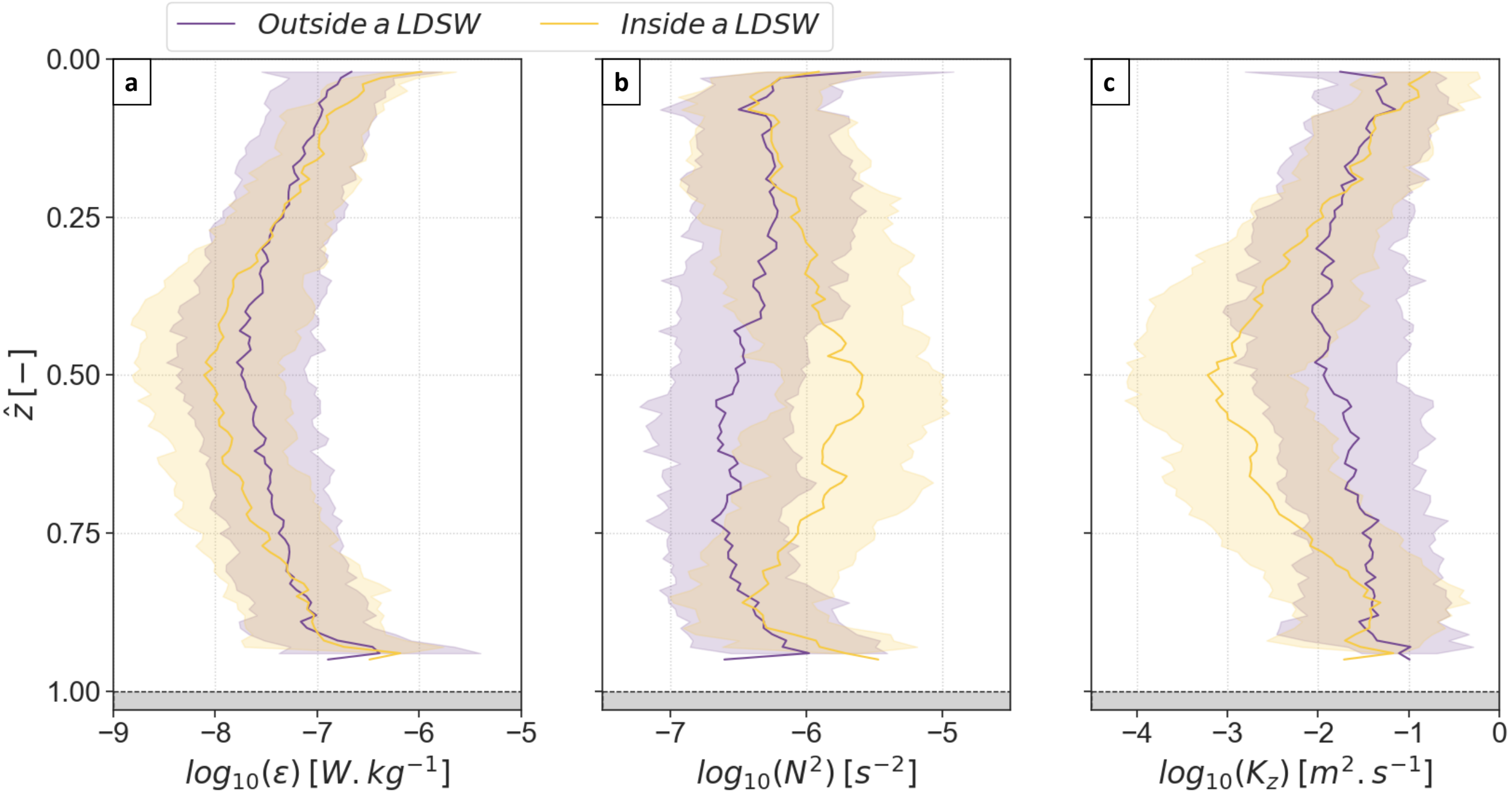
Outside a LDSW
Inside a LDSW
a
b
c
0.00
0.25
0.50
0.75
1.00
$\hat{z}$ [−]
−9
−8
−7
−6
−5
$log_{10}(\varepsilon)\,[W.kg^{-1}]$
−7
−6
−5
$log_{10}(N^2)\,[s^{-2}]$
−4
−3
−2
−1
0
$log_{10}(K_z)\,[m^2.s^{-1}]$

Figure 12.

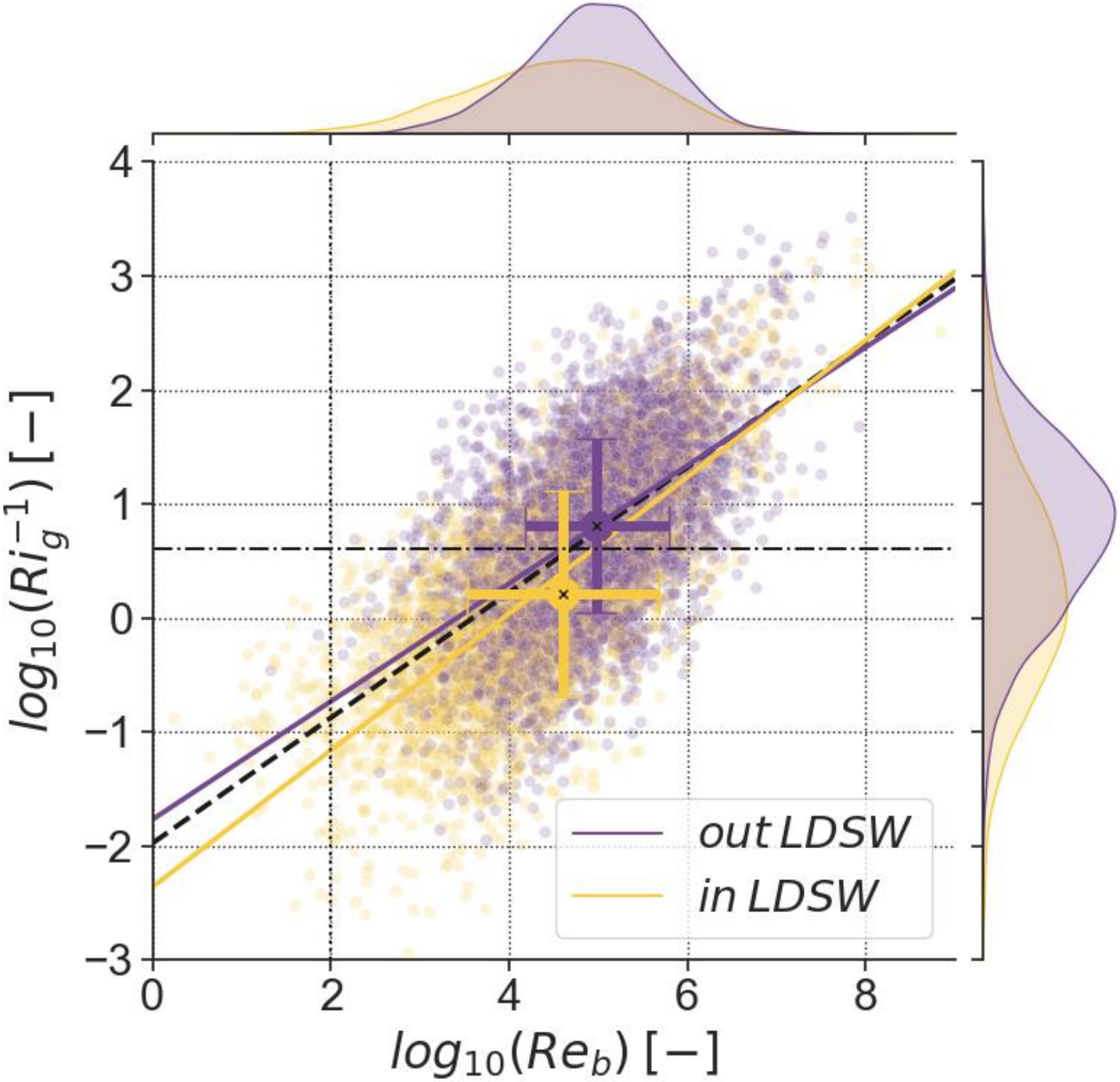
4
3
2
1
0
−1
−2
−3
0
2
4
6
8
$log_{10}(Ri_g^{-1})$ [−]
$log_{10}(Re_b)$ [−]
out LDSW
in LDSW

Figure 13.

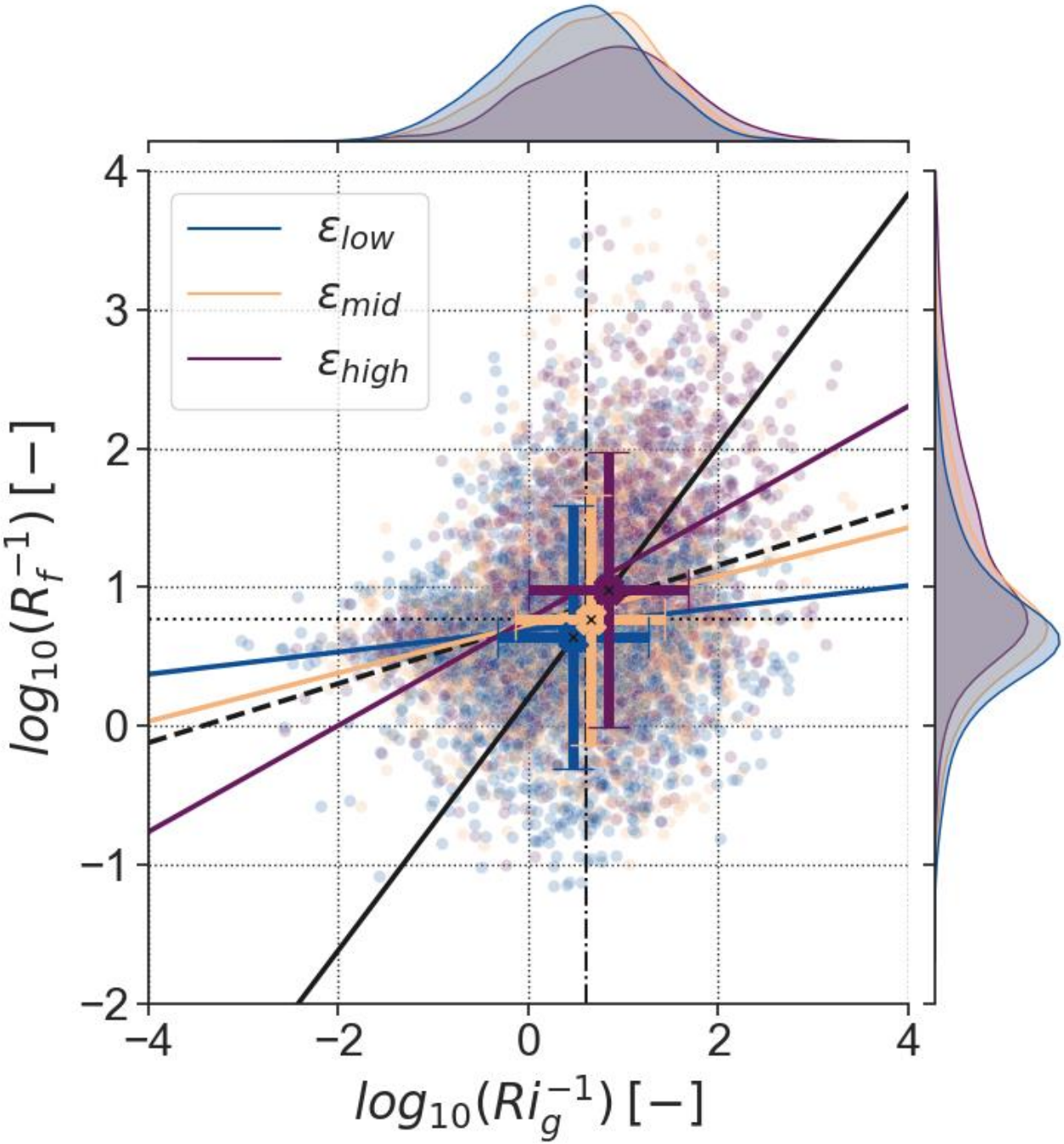
ε_{low}
ε_{mid}
ε_{high}
$log_{10}(R_f^{-1})$ [−]
$log_{10}(Ri_g^{-1})$ [−]
4
3
2
1
0
−1
−2
−4
−2
0
2
4